Spatiotemporal dynamics and optical vortices in a photorefractive phase-conjugate resonator

by
Siuying Raymond Liu
and
Guy Indebetouw

Physics Department
Virginia Polytechnic Institute and State University
Blacksburg, VA 24061-0435

Abstract

A truncated modal expansion approach is used to study the spatiotemporal dynamics of a phase-conjugate resonator as a function of Bragg detuning. The numerical results reveal a rich variety of behaviors. Emphasis is given to the spatial distribution of optical vortices, their trajectories and their relationship to the beam's spatial coherence. The limitations of the model are discussed and experimental results are presented for comparison with the model's predictions and assessment of its soundness.

1 Introduction

Nonlinear dynamics in optical systems (e.g.: passive cavities, wave mixing geometries and lasers) have been the subject of intense research during the past few decades. The interest stems from the many potential applications of such devices in e.g. optical bistability, phase conjugation, image processing, etc. All these applications involve the two dimensional (2-D) transverse nature of the system in a fundamental way [1]. Yet, although the nonlinear and chaotic behavior of low-dimensional systems described by ordinary differential equations (ODE) is fairly well understood [2, 3], problems that include the transverse dimensions and are described by systems of partial differential equations (PDE) remain a theoretical challenge and do not benefit from well established experimental methodologies [4]. Furthermore, their numerical analyses require large computational budgets [5, 6].

The system considered in this paper is the phase-conjugate resonator (PCR) sketched in fig. 1. It consists of a phase-conjugate mirror (PCM) and a self-imaging cavity made of a lens and a planar mirror. PCRs have interesting potential applications in image storage and processing [7, 8, 9] as well as in laser systems [10]. The particular geometry of fig. 1 was chosen because it leads to simple boundary conditions and because certain aspects of its dynamics derived numerically [11] as well as experimentally [12, 13] have already been reported in the literature, providing a useful comparative reference frame. In addition, the PCR of fig. 1 may offer a convenient way of studying experimentally some as yet partially understood aspects of more generic dynamical systems. For example, the transverse confinement of the resonator is conveniently controlled by the size of two apertures which determine the cavity Fresnel number. This is akin to controlling the aspect ratio in hydrodynamics and thus offers

a possible way of studying the transition between low aspect ratio dynamics involving few modes to larger aspect ratio systems where dislocations, vortices and defects play a dominant role [14]. An additional motivation for this work is that experimental and numerical studies of many different physical systems are needed to determine possible universal behaviors and test theoretical conjectures, e.g. the similar role played by topological defects in different physical systems and the striking analogies between laser dynamics and hydrodynamics [15, 16, 17].

This paper has two aims. The first is to describe and establish the soundness of a somewhat arbitrary yet sensible modal decomposition approach to study the dynamics of PCRs with modest Fresnel numbers. This is done by comparing numerical results with actual experimental data. The hope is that this comparison, although complicated by the difficulty in measuring experimental control parameters exactly and by the problematic effect of stochastic noise, will prove sufficiently convincing to confirm the usefulness of the approach. The second is to illustrate the relationship existing between the dynamics of the optical vortices observed in PCRs [12, 13, 17] and the spatial correlation of the oscillating beam.

The paper is organized as follow. The PCR's equations and boundary conditions within approximations compatible with experimental conditions are stated in section 2.1. Arguments justifying the modal expansion approach are given in section 2.2 and the method is then used to arrive at a set of modal amplitude equations. In section 3.1, a particular set of parameter values is chosen and the system is integrated, using the off-Bragg detuning as a control parameter. Different dynamical behaviors are identified from local time series, power spectra and phase space portraits. Examples of vortices' motions and spatial correlation maps are given in section 3.2. Experimental results are presented and discussed in section 4

and a summary is given in section 5.

2 The model

2.1 Phase-conjugate resonator

The PCR is sketched in fig. 1. Its active element is an externally pumped photorefractive medium acting as a PCM. Maxwell's equations for the optical field in the medium lead to the following coupled equations:

$$\left(\frac{j\nabla_T^2}{2k} + \hat{k}_1 \cdot \nabla + \alpha + \frac{\partial}{v\partial t}\right) A_1(x,y,z,t) = -Q(x,y,z,t)A_4(x,y,z,t)e^{-jbz}, \tag{1}$$

$$\left(-\frac{j\nabla_T^2}{2k} + \hat{k}_2 \cdot \nabla + \alpha + \frac{\partial}{v\partial t}\right) A_2^*(x,y,z,t) = Q(x,y,z,t)A_3^*(x,y,z,t), \tag{2}$$

$$\left(\frac{j\nabla_T^2}{2k} + \hat{k}_3 \cdot \nabla + \alpha + \frac{\partial}{v\partial t}\right) A_3(x,y,z,t) = -Q(x,y,z,t)A_2(x,y,z,t), \tag{3}$$

$$\left(-\frac{j\nabla_T^2}{2k} + \hat{k}_4 \cdot \nabla + \alpha + \frac{\partial}{v\partial t}\right) A_4^*(x,y,z,t) = Q(x,y,z,t)A_1^*(x,y,z,t)e^{-jbz}, \tag{4}$$

where, in spirit of the slowly varying envelope approximation, the field in the medium is written as

$$E(x,y,z,t) = \sum_{i=1}^{4} A_i(x,y,z,t)e^{j(\omega t - \vec{k}_i \cdot \vec{r})} + \text{ c.c.}, \tag{5}$$

$v = c/\bar{n}$ is the speed of light in the medium. $\bar{n}$ is the average refractive index. $\vec{k}_i$ are unit vectors pointing in the direction of the four wavevectors in the medium. The wavenumber is $k_i = \omega/v$ where ω is the angular frequency of the pump and α is the linear absorption coefficient. ∇_T is the transverse gradient operator. The parameter b is the wavevector mismatch (momentum mismatch along the z-axis) measuring the departure from the Bragg

condition. This off-Bragg parameter is introduced as a means of varying the amount of phase transfer between the waves mixed in the nonlinear medium and is later taken as the control parameter.

The equation for the phase grating Q is derived from the standard band transport model of Kukhtarev [18] and reads, in the single grating approximation,

$$\tau\frac{\partial Q(x,y,z,t)}{\partial t}+C_1Q(x,y,z,t)=\gamma_o C_2\left(\frac{A_1(x,y,z,t)A_4^*(x,y,z,t)e^{jbz}+A_2^*(x,y,z,t)A_3(x,y,z,t)}{I_o(x,y,z,t)}\right), \tag{6}$$

where $C_1=(E_D+E_q+jE_o)/(E_M+E_D+jE_o)$ and $C_2=[(E_q+E_D)/E_D][(E_D+jE_o)/(E_M+E_D+jE_o)]$.$\tau$ is the Debye relaxation time. E_D, E_q and E_M are characteristic fields (diffusion, limiting space charge and drift field respectively) which depend on the medium properties and the grating spatial frequency. E_o is an external or photovoltaic field, I_o is the average light intensity in the medium and γ_o a coupling constant function of the geometry and the electro-optic tensor of the medium.

The boundary conditions for the wave equation in the medium are determined by the cavity geometry. The transverse confinement of the cavity is controlled by two square apertures H_1 and H_2 of sides $2a_{pcm}$ and $2a_m$ respectively. The first aperture is located near the phase-conjugate mirror in the front focal plane of the lens (fig. 1). The second one is in the back focal plane of the lens next to the planar mirror. The transverse confinement is measured by the cavity Fresnel number defined as

$$\mathcal{F}=2a_m a_{pcm}/\lambda f, \tag{7}$$

where λ is the wavelength in vacuum and f the focal length of the lens.

One cavity round trip, starting at the PCM consists of a truncation by H_1 and imaging in a 4-f afocal system with a pupil H_2. Thus, the amplitude A_4 is proportional to the truncated convolution of A_3 with a point-spread-function which is the Fourier transform of the aperture H_2. Using transverse coordinates normalized to the aperture size a_{pcm}, the boundary condition at the entrance face ($z = 0$) of the PCM, which is also the plane of the aperture H_1 becomes

$$A_4(x,y,0,t+2L/c) = r\mathcal{F}^2\mathrm{rect}(x/2)\mathrm{rect}(y/2)\iint_{-1}^{+1} A_3(x',y',0,t)\mathrm{sinc}\left[\mathcal{F}(x'+x)\right] \mathrm{sinc}\left[\mathcal{F}(y'+y)\right] dx'dy', \tag{8}$$

where $\mathrm{rect}(x/2) = 1$ for $-1 \leq x \leq 1$ and $= 0$ otherwise, $\mathrm{sinc}(x) = \sin(\pi x)/\pi x$ and r is the amplitude reflection coefficient of the planar mirror. L is the cavity optical length and an unimportant phase factor has been omitted in eq. 8.

The experimental conditions pertaining to section 4 are those of a slow photorefractive medium (e.g. $BaTiO_3$). In these conditions, equations 1- 4 can be further simplified by neglecting the temporal derivative on the left hand sides. The round trip time delay in the boundary condition is also neglected for the same reason.

2.2 Modal decomposition

The direct integration of equation 1- 6 requires a large computational budget. Furthermore, calculations taking only one transverse dimension into account, althougth showing interesting dynamical behaviors (e.g. ref. [11]), fail to reveal the crucial role played by the phase defects in mediating the spatiotemporal dynamics of the PCR [12, 13, 17].

Modal decomposition is a powerful tool for studying systems of PDEs [19]. This approach allows one to reduce an infinite dimensional problem to a finite (hopefully low) dimensional problem described by a system of equations for the modal coefficients. The success of the method relies on the assumption that the dynamics is fairly well described by the interaction of a small number of active spatial modes. The main difficulty resides in the choice of appropriate basis functions for the expansion. They must accurately represent the spatial structure of the active modes. However, this structure is generally difficult to identify *a priori* and one often relies on the choice of a sensible basis rather than trying to identify the exact optimal basis.

In optical resonators with relatively small Fresnel numbers, these simplifications appear to be justified. The dynamics of these systems is indeed dominated by a few active modes and the Gauss-Laguerre or Gauss-Hermite modes of the empty resonator seem to be reasonable basis functions to replace the optimal ones [20]. Of course such a practice introduces a degree of arbitrariness since a small number of modes of the sensible basis may not be sufficient to adequately represent the spatial structure. Nevertheless, the resulting enormous reduction of computational budget and the physical insight that can be gained justify further tests of the validity of this approach.

The cavity fields A_3 and A_4 in the nonlinear medium ($0 \leq z \leq d$) are thus expanded in series as

$$A_3(x,y,z,t) = \sum_{m,n} f_{3mn}(z,t) u_m^*(x,z;z_o) u_n^*(y,z;z_o) \tag{9}$$

$$A_4(x,y,z,t) = \sum_{m,n} f_{4mn}(z,t) u_m(x,z;z_o) u_n(y,z;z_o) \tag{10}$$

and the Gauss-Hermite modes are chosen as a sensible set for the decomposition:

$$u_m(x,z;z_o) \equiv \left(\frac{2}{\pi}\right)^{1/4}[2^m m! w(z)]^{-1/2} H_m\left(\frac{\sqrt{2}x}{w(z)}\right) \exp\left[-\frac{x^2}{w^2(z)} - j\frac{kx^2}{2R(z)} + j(m+1/2)\tan^{-1}(z/z_o)\right], \tag{11}$$

where H_m are Hermite polynomials. The beam radius is $w(z) = w_o(1 + z^2/z_o^2)^{1/2}$, its radius of curvature is $R(z) = z(1 + z_o^2/z^2)$. $z_o = \pi w_o^2 \bar{n}/\lambda$ is the Rayleigh distance and $k = 2\pi\bar{n}/\lambda$ is the wavenumber in the medium. The waist is located at the entrance face of the PCM ($z = 0$).

The pump beams are Gaussian with a waist w_p chosen sizably larger than w_o and for simplicity are assumed to make a very small angle with the z-axis. Thus, the pump beams are

$$A_1(x,y,z,t) = f_1(z,t)U(x,z)U(y,z) \tag{12}$$

$$A_2(x,y,z,t) = f_2(z,t)U^*(x,z)U^*(y,z) \tag{13}$$

where $U(x,z) = u_o(x,z;z_p)$ and $z_p = \pi w_p^2 \bar{n}/\lambda$.

The series in equations 9, 10 are infinite and the problem remains infinite dimensional. Because of the cavity transverse confinement however, we expect that only the modes with indices smaller than some upper bound will take a significant part in the dynamics. The cavity Fresnel number defined by equation 7 is a measure of the amount of transverse spatial information that the cavity can accommodate ($\mathcal{F}^2$ is the space-bandwidth product of the cavity). It is thus reasonable to assume that only the modes with indices smaller than $\mathcal{F}$ will play a dominant role in the wave interaction in the PCM since they are the modes which are most likely to survive in the cavity. It must be stressed however that choosing which modes to include in the dynamics is somewhat arbitrary. Only a comparison with experiment can

provide a *a posteriori* justification of this choice. The important point is that the series of equations 9,10 can often be limited to a small number of terms while still giving results which agree at least qualitatively with observations, as will be shown in a later section.

Equations 9- 13 are substituted in 1- 6 and use is made of the fact that the Gauss-Hermite modes are solutions of the Helmholtz equation:

$$\left(\frac{j\nabla_T^2}{2k} + \frac{\partial}{\partial z}\right) u_m(x,z)u_n(y,z) = 0, \tag{14}$$

and satisfy the biorthogonality relation [21]

$$\iint_{-\infty}^{+\infty} dxdy u_m(x,z)u_n(y,z)u_p^*(x,z)u_q^*(y,z) = \delta_{mp}\delta_{nq}. \tag{15}$$

A final set of differential equations is then obtained for the modal amplitudes:

$$\frac{\partial f_1(z,t)}{\partial z} + \alpha f_1(z,t) = -e^{-jbz}\sum_{m,n} f_{4mn}(z,t)h_{mn}(z,t), \tag{16}$$

$$\frac{\partial f_2^*(z,t)}{\partial z} - \alpha f_2^*(z,t) = \sum_{m,n} f_{3mn}^*(z,t)h_{mn}(z,t), \tag{17}$$

$$\frac{\partial f_{3mn}(z,t)}{\partial z} - \alpha f_{3mn}(z,t) = f_2(z,t)h_{mn}(z,t), \tag{18}$$

$$\frac{\partial f_{4mn}^*(z,t)}{\partial z} + \alpha f_{4mn}^*(z,t) = e^{-jbz} f_1^*(z,t)h_{mn}(z,t), \tag{19}$$

where

$$h_{mn}(z,t) = \iint_{-\infty}^{+\infty} dxdy Q(x,y,z,t)u_m(x,z)u_n(y,z)U^*(x,z)U^*(y,z) \tag{20}$$

is the overlap integral of the pump and the projection of the grating Q onto the mode (m,n).

The grating equation 6 is likewise projected onto the cavity modes to obtain

$$\tau\frac{\partial h_{mn}(z,t)}{\partial t} + C_1 h_{mn}(z,t) = \gamma_o C_2 \{e^{jbz} f_1(z,t)\sum_{k,l} f_{4kl}^*(z,t)G_{klmn}(z,t) + f_2^*(z,t)\sum_{k,l} f_{3kl}G_{klmn}(z,t)\}, \tag{21}$$

with

$$G_{klmn}(z,t) = \iint_{-\infty}^{+\infty} \frac{u_k^*(x,z)u_l^*(y,z)u_m(x,z)u_n(y,z)|U(x,z)|^2|U(y,z)|^2}{I_o(x,y,z,t)}dxdy \qquad (22)$$

and the total intensity $I_o(x,y,z,t)$ is calculated using equations 9, 10, 12, 13.

The integration of equations 16- 22 is greatly simplified if the interaction length in the PCM is shorter than all the beams' Rayleigh distances:

$$d \ll z_o, z_p. \qquad (23)$$

In this case, diffraction can be neglected in the medium and the interacting beams' modes, normalized to the aperture size a_{pcm}, take the simple form:

$$u_m(x,z;z_o) \simeq u_m(x) = \left(\frac{1}{\pi}\right)^{1/4}\left(\frac{\beta_o}{2^m m!}\right)^{1/2} H_m(\beta_o x)e^{-\beta_o^2 x^2/2}, \qquad (24)$$

with $\beta_o = \sqrt{2}a_{pcm}/w_o$. The pumps are gaussian with a parameter $\beta_p = \sqrt{2}a_{pcm}/w_p$.

The boundary conditions for the modal amplitudes at $z = 0$ are found from equation 8 using the modal decompositions 9, 10. They read

$$f_{4mn}(0,t) = r\mathcal{F}^2 \sum_{k,l} f_{3kl}(0,t)I_{km}I_{ln}, \qquad (25)$$

with

$$I_{km} = \int_{-1}^{+1} dx \mathcal{H}_k(x)u_m(x), \qquad (26)$$

and

$$\mathcal{H}_k(x) = \int_{-1}^{+1} dx' u_k(x')\mathrm{sinc}[\mathcal{F}(x'+x)]. \qquad (27)$$

The algorithm described by Solymar in [22] was used to solve the system of equations 16- 22 with the boundary conditions 25- 27. Some results are illustrated in the next section.

3 Numerical results

Phase transfer between interacting beams in the four-wave mixing process appears to be a desirable condition for the observation of non trivial dynamics with reasonable values of the coupling parameter. For example, the onset of instabilities in ring resonators with injected signals has been shown to depend sensitively on this parameter [23]. In a material having a real coupling parameter and no external field, this phase transfer can be the result of an angular mismatch of the pump beams. For the simulation presented in this section, the control parameter was chosen to be the phase mismatch bd (off-Bragg parameter), where b is the momentum mismatch along z and d is the length of the nonlinear medium.

In a recent report [13], it was shown that the dynamics of the PCR strongly depends on the cavity Fresnel number. Increasing the Fresnel number relaxes the transverse confinement of the system and allows higher order modes to take part in the dynamics. As a result, the spatial complexity of the beam increases. In particular, the number of vortices increases and their motion becomes more complex, eventually leading to chaotic states and in the limit of large Fresnel numbers, to spatiotemporal turbulence. The example shown in the next section is for a Fresnel number $\mathcal{F} = 3.5$. This is small enough so that only a few modes are expected to take part in the dynamics, yet it is large enough to exhibit a wide range of behaviors.

Experiments carried out with Fresnel numbers between 3 and 4 reveal a transverse pattern in which two pairs of defects of opposite charges repetitively nucleate, move along symmetrical trajectories, spending much time in some circular zone centered on the beam and disappear at boundaries or collide and annihilate each other [13]. Based on these observations

and in order to keep the computational budget to a minimum, it was decided to limit the expansions in eqs. 9, 10 to four modes only, namely, $(m,n) = (0,0),(1,1),(2,0)$, and $(0,2)$ with a beam waist $w_o = a_{pcm} = 1$.

As already mentioned, there is a certain degree of arbitrariness in this choice. However, with a Fresnel number of 3.5, it is unlikely that modes with indices higher than 3 can survive in the cavity and play a significant role in the dynamics. Indeed, when a mode of higher index was initially added to the series, the simulation showed that its amplitude decays and vanishes with the other transients. Another reason for limiting the expansion to these particular four modes is that it allows the calculation of the vortices' positions to be done algebraically rather than numerically, thus saving CPU time. Finally, simulations ran with different choices of modes, although giving result which differ in details, revealed the same generic range of behaviors.

The other parameters of the model are chosen as follow: $\gamma d = -10, \alpha d = 0.15, \beta_o = \sqrt{2}, \beta_p = \sqrt{2}/10, E_D = 1kV/cm, E_q = 5kV/cm, E_M = 100kV/cm, E_o = 0$ and the pump beams intensity coefficients are $f_1^2(z=0) = f_2^2(z=d) = 0.5$. As an initial condition, it is assumed that the four modes are excitied from white noise and have initial modal amplitudes $f_{4mn}(t=0) = 10^{-4}$.

3.1 Local intensity fluctuations

The local intensity of the cavity field A_4 measured at the exit face of the PCM was chosen as a variable because it is easily accessible experimentally. The local intensity $I_4(x_o, y_o, d)$ was calculated at $(x_o, y_o) = (0.75, 0.15)$ in a region where experiments indicate that the intensity

fluctuations have a deep modulation. Figure 2 shows short sections of time series of the local intensity fluctuations for different values of the off-Bragg parameter. Time in fig. 2 is normalized to the relaxation time τ' of the photorefractive grating ($\tau' = |(E_M + E_D + iE_o)/(E_D + E_q + iE_o)|\tau$).

After the transients have vanished and a stationary state has been reached, the local extrema of these time series were recorded and used to construct the bifurcation diagram of fig. 3. For small Bragg mismatch ($|bd| < 2.4$) the motion is periodic. Unstable oscillations occur in a wide range of parameter values ($3.6 < |bd| < 2.4$). In most of this range the motion appears to be quasiperiodic. Although this is not readily visible at the resolution of fig. 3, some regions of the bifurcation diagram seem to be more chaotic than others and there exist narrow windows in which the motion is periodic, usually showing a large number of subharmonics. For $|bd| > 3.6$, the motion is periodic again and eventually, with a sufficiently large mismatch, the only stable state is $I_4 = 0$.

The time series of fig. 2 were chosen to illustrate these various types of motion. The corresponding power spectra shown in fig. 4 give a fair indication of the dynamics of the system. Additional information can be gained by reconstructing pseudo phase space portraits such as these shown in fig. 5 which are plots of the imaginary part of the field $A_4(x_o, y_o, d)$ versus its real part.

At $bd = -2.3$, the motion is clearly periodic with a frequency f_1 slightly larger than 1/2 relaxation rate of the grating (fig. 4a) and the phase space portrait (fig. 5a) is a limit cycle. At $bd = -2.45$, a second characteristic frequency f_2, about 1/10 grating relaxation rate, appears and modulate the time series (figs 2b and 4b). For this value of the off-Bragg

parameter, the two frequencies are incommensurate and the motion is quasiperiodic with the phase space portrait shown in fig. 5b. At $bd = -2.55$, the low frequency modulation deepens (fig. 4c) and more energy shifts toward higher harmonics of f_1 and linear combinations of the two main frequencies (fig. 4c). The phase space portrait still shows some structures although it will eventually densely fill a region of phase space since the two frequencies are still incommensurate. At $bd = -2.75$, the time series is more irregular, possibly chaotic (fig. 2d). There are still two main frequencies but the spectrum is broadened and shows a number of additional peaks indicating the presence of a third frequency about $1/100$ grating relaxation time (fig. 4d). The phase space portrait of fig. 5d is diffuse and show no apparent structure. At $bd = -3.18$, a phenomenon akin of frequency locking occurs. The two larger frequencies pull each other as to become rational. The very low frequency, which seems to have appeared only to allow this locking to occur, disappears. The spectrum of fig. 4e shows a ratio $f_1/f_2 = 13$. The periodic motion with 13 subharmonics is confirmed by the closed loop phase space trajectory of fig. 5e.

3.2 Vortices and spatial correlation

The local intensity fluctuations offer a convenient means of comparing model predictions with experimental data but this information is not sufficient to fully characterize the spatiotemporal dynamics. The aim of this section is to illustrate the role played by the phase defects (vortices) in mediating the dynamics.

The vortices appear where the real and imaginary parts of the field amplitude vanish simultaneously. For example, fig. 6 shows a snapshot of the beam crosssection $I_4(x, y, d)$ for

$bd = -2.45$, which exhibits four dark spots. The corresponding phase contour diagram of fig. 7 clearly identifies these spots as two pairs of vortices of opposite charges (± 1). In time, these vortices nucleates, move around, annihilate each other or disappear at boundaries. This is the motion of the vortices which gives rise to the local intensity fluctuations described in the previous section. This section gives a more detailed illustration of the spatial aspect of the dynamics and attempts to identify the spatial features responsible for the characteristic frequencies observed in the local times series.

Figure 8a to e shows the temporal evolution of the field amplitude $A_4(x = 0.75, y, d)$ along a line across the beam for the same off-Bragg parameter values used in figs. 2, 4, 5. For a small offset ($bd = -2.3$), all points across the line execute synchronized periodic motions with a period a bit smaller than two grating time constants (fig 8a). In 2-D, the phase of the wavefront is observed to breathe periodically together with the amplitude but the phase gradients produced are not steep enough to trigger the nucleation of defects.

At $bd = -2.45$ (fig 8b), the periodic motion is transversely modulated with a period of the order of 10 grating time constants. This spatial motion gives rise to the quasiperiodic time series of fig. 2b. In 2-D, the phase gradients are locally steep enough to tear the wavefront at locations where two pairs of defects of opposite charges nucleate. The four vortices then travel across the wavefront, pairs of opposite charge collide and annihilate. The higher frequency of the time series seems to correspond to the recovery rate of the local wavefront after a vortex has moved through it, while the lower frequency corresponds to the full cycle of vortices' nucleation, motion and annihilation. At $bd = -2.55$, the motion is similar to that just described but with deeper modulation (fig. 8c, which is plotted with a

different time scale).

At $bd = -2.75$ (fig. 8d), the transverse modulation is irregular, possibly due to the occurrence of a third incommensurate frequency. In 2-D, in contrast with the previous case where the vortices' trajectories were confined to fairly well defined area, they now seem to visit the whole beam crosssection irregularly. At $bd = -3.18$ (fig. 8e) the motion is periodic again. The transverse modulation has a period of ~ 23 grating time constants, which is 13 times the period of $\sim 9/5$ time constant of the fast oscillations measured in fig. 8a.

The remainder of this section gives a more detailed illustration of the relationship between the vortices' trajectories and the spatiotemporal coherence of the beam. The dynamics of the fluctuating beam can be characterized by a correlation index distribution. The correlation index between two points (x_1, y_1) and (x_2, y_2) is defined as the maximum, with respect to a temporal shift Γ, of the correlation of the intensity fluctuations at these two points. i.e.

$$C(x_o, y_o; x, y) = \text{MAX}\left[\frac{< (I_1(t) - < I_1 >)(I_2(t+\Gamma) - < I_2 >) >}{[< I_1^2 > - < I_1 >^2]^{1/2}[< I_2^2 > - < I_2 >^2]^{1/2}}\right] \qquad \forall\Gamma, \qquad (28)$$

where $I_i(t) = I(x_i, y_i, t); i = 1, 2$. Stationarity is assumed and $< \cdot >$ represents a time average. The correlation index is high whenever the intensity fluctuations are highly correlated even in the presence of a time delay. Such time delays may be expected if the fluctuations are due to features (e.g. vortices) travelling across the beam as waves.

To illustrate the usefulness of this concept, the correlation index distribution with respect to the origin, $C(0, 0; x, y)$, was calculated for the five off-Bragg parameter values used in the previous examples. The spatial correlation diagram thus obtained can then be compared with the vortices' trajectories. For this, the positions of the vortices were calculated

at regular intervals of time by solving for $\mathrm{Re}A_4(x,y,t) = \mathrm{Im}A_4(x,y,t) = 0$ and represented by dots on a 2-D plot. Note in passing that with the particular, apparently arbitrary choice of modes adopted for the expansion of A_4, this could be solved algebraically.

Figure 9 shows the correlation index distribution for a small value of the off-Bragg parameter ($bd = -2.3$). No vortices appear in the field but the amplitude and phase of the wavefront oscillate periodically as if waves were travelling along an annular area centered on the beam.

At $bd = -2.45$, the motion is characterized by the nucleation of two pairs of defects at two ends of a diagonal. The vortices move along circular trajectories and the members of opposite charges of each different pairs collide and annihilate near the two ends of the opposite diagonal. This motion is then repeated periodically with alternating directions. A sequence of interferogram snapshots illustrating this motion is shown in fig. 10. A plot showing the distribution of vortice's positions in time is shown in fig. 11a. The vortices' trajectories are clearly confined to a narrow annular area in the beam. Figure 11b shows the corresponding correlation index distribution. Its particular shape can be explained by the fact that the intensity fluctuations at some location in the beam are due to the passage of a vortex nearby, that no vortex ever appears near the origin (the fixed point for calculating C) and that the vortices' trajectories are confined to a narrow annular region of space. It is only near this region that the correlation index is expected to drop sharply. The correlation index distribution was also calculated with a fixed point chosen at a location frequently visited by a vortex. The distribution looked as a negative of fig. 11a. The correlation index is high in the annular area visited by the vortices and low everywheree else. This confirms

that the four vortices appearing in the pattern are highly correlated, as is expected since they nucleate simultaneously and produce intensity fluctuations near their trajectories which are only delayed in time. A qualitatively similar behavior of the vortices was observed for $bd = -2.55$, as illustrated in fig. 12a and b.

An apparently chaotic time series was observed for $bd = -2.75$. Figure 13a shows that the vortices' position distribution is diffuse, indicating that their trajectories do not remain confined in narrow regions of space. In fact, the defects can visit about any place in the beam except near the origin and this is only because of the peculiar set of modes chosen for the decomposition. The corresponding correlation index distribution shown in fig. 13b is low in all regions visited by the vortices. Figure 13c shows the correlation index distribution with a fixed point $(x_1, y_1) = (1, 0.3)$ frequently visited by a vortex. It shows that even though the vortices trajectories have become more random, the intensity fluctuations in the regions they visit remain highly correlated.

At $bd = -3.18$, an apparent frequency locking was observed in the local intensity time series, leading to a quieter dynamics. For this value of the off-Bragg parameter, the wavefront phase and amplitude oscillate periodically but no defects nucleates. The regions in space where these fluctuations occur are identified as two concentric rings in the interferogram snapshots of fig. 14 and in the corresponding correlation index distribution of fig. 15.

4 Experimental results

The experimental apparatus has been described in details in a previous report [13]. The PCM is an externally pumped single crystal of $BaTiO_3$. The source for the pumps is a single mode

Ar ion laser ($\lambda = 514nm$) optically isolated from the setup by a Faraday rotator. The cavity ends with a planar dielectric mirror (R=0.95%) and contains a 16cm focal length lens. Two intra-cavity circular apertures of diameter d_{pcm} = 0.79mm and d_m =0.38mm give a Fresnel number $\mathcal{F}$ = 3.7. The off-Bragg parameter was varied by tilting the mirror directing the pump A_1 toward the PCM and its values were calculated as the product of the momentum mismatch along the cavity axis with the interaction length. The change in pump overlap due to the tilting was measured and found negligible.

The aim of the experiments is to show by way of illustrations, that the range of behaviors predicted by the model and described in section 3 is indeed observed in the physical system. It would be unrealistic to expect a quantitative match between the experimental data and the results of numerical simulations if only because it is not possible to control experimentally which modes are actually taking part in the dynamics. A qualitative match however, would at least indicate that the truncated modal expansion approach gives a fair representation of the actual dynamics of the PCR.

Figure 16 shows an interferogram snapshot of the beam exiting the PCM. It exhibits four vortices located at the corners of a quadrangle in an arrangement similar to that predicted by the model in fig. 6 and 10.

The off-Bragg parameter was scanned between two extreme values at which the momentum mismatch is large enough to reduce the gain below cavity losses and prevent oscillation. Local time series were recorded within that range and analyzed using power spectra and delayed time phase space portraits. Near the center of the covered range of parameter values, a region where the motion was clearly periodic could be identified. On both sides of

this region, similar sequences of various dynamical behaviors were observed, up to large mismatches at which the cavity stops oscillating. Before reaching these limits, simple periodic oscillations at reduced amplitudes were again observed. The sequence of behaviors just described is exactly what the bifurcation diagram of fig. 3 would predict (note that within the approximations of the model, this bifurcation diagram is symmetrical around $bd = 0$ but in the actual setup, this symmetry is broken). By analogy with the model, the origin of parameter space ($bd_r = 0$) was chosen as the midpoint of the central region showing periodic oscillations. Other values of the off-Bragg parameter mentioned below are relative to this point. Some examples of time series are shown in fig. 17 and the corresponding power spectra are displayed in fig. 18. These examples were chosen to illustrate the variety of dynamical behaviors exhibited by the PCR and to compare them with the characteristic behaviors predicted by the model.

Figures 17a, 18a show the periodic motion expected for small values of the off-Bragg parameter. The corresponding delayed time phase space portrait (fig. 19a) shows broadening which may give an indication of the level of stochastic noise (although in our case there is no sure way of differentiating between a limit cycle broadened by stochastic noise and a strange attractor with a natural width due to the dynamics).

Figures 17b, 18b obtained with $bd_r = 0.65$ show a chaotic state with an irregular time series and a spectrum containing at least two or three incommensurate frequencies, including the main frequency of about 0.14Hz, and a large continuum, a signature of chaos. The exponential decay of the power spectrum (linear on the semilog scale of fig. 18 may be indicative of deterministic chaos). The corresponding phase space portrait of fig. 19b is

diffuse and featureless.

Figures 17c, 18c give a typical example of frequency locking obtained at $bd_r = 1.29$. The locking at period three is confirmed by the closed-loop phase space trajectory shown in fig. 19c. Note that the width of this limit cycle is about the same as that of fig. 19a and is probably due to stochastic noise.

At $bd_r = 1.94$ (figs. 17d, 18d) the motion is quasiperiodic with a spectrum containing only two incommensurate frequencies and their linear combinations. Another quasiperiodic motion obtained at $bd_r = 2.16$ is shown in fig. 17e, 18e. Here the lower frequency appears as sidebands of the higher one. For larger values of the off-Bragg parameter, e.g. $bd_r > 2.37$, the motion is periodic again with the same dominant frequency of ~ 0.14Hz but with decreasing amplitude. When $bd_r > 3$, the gain is lower than the cavity losses and no oscillation occurs.

5 Summary and conclusions

A model based on a truncated expansion of the field into cavity modes has been tested to describe the spatiotemporal dynamics of a phase-conjugate resonator. The Gauss-Hermite modes of the empty cavity are chosen as sensible basis functions to represent the fields in the nonlinear medium. Although the choice of the modes which take parts in the dynamics is arbitrary in this method, justifications are given for truncating the series at a mode index of the order of the cavity Fresnel number. Verifications of the validity of this choice are later given by comparison with experimental data. Numerical examples, using the off-Bragg parameter (momentum mismatch) as a control parameter reveal a rich variety of dynamical

behaviors illustrated by the local intensity fluctuations and ranging from simple periodic oscillations to quasiperiodic motions and chaotic states.

The modal decomposition method is particularly well suited to study the spatial aspect of the dynamics without requiring prohibitive computational budgets. Numerical results indicates that the spatiotemporal dynamics of the PCR is mediated by the nucleation of pairs of defects of opposite charges in the beam and by their subsequent motion and annihilation. Maps of the spatial coherence function of the beam are found to be templates of the corresponding maps of the vortices' trajectories, establishing a strong correlation between these two quantities. The loss of temporal coherence and the onset of temporal chaos in the local intensity fluctuations is likewize correlated to the loss of spatial confinement of the vortices' trajectories and the loss of spatial coherence.

Experimental data obtained with a PCR using an externally pumped $BaTiO_3$ photorefractive PCR reveal a range of dynamical behaviors similar to those shown by the simulation. These results confirm and complete the findings of earlier experimental studies of the PCR's dynamics at various Fresnel number [13]. The arbitrariness of choice of the modes to include in the dynamics is the main shortcomming of the truncated modal expansion approach used in this work. Nevertheless it appears to be a convenient and computationally nondemanding tool to study and predict qualitatively the spatiotemporal behavior of phase-conjugate resonators and perhaps of other nonlinear optical devices as well.

The authors wish to acknowledge the financial support of NASA/Langley for the research leading to this report. In particular, we recognize the assistance of Sharon Welch and David Cox of the Spacecraft Control Branch in providing adequate computing facilities for

this research.

References

[1] N. B. Abraham and W. J. Firth, "Overview of transverse effects in nonlinear optical systems," *J. Opt. Soc. Am.*, **B 7**, pp. 951–962, 1990.

[2] P. Berge, Y. Pomeau, and C. Vidal, *Order within Chaos.* John Wiley and Sons, New York, 1984.

[3] C. O. Weiss and R. Vilaseca, *Dynamics of lasers.* VCH Pulbisher Inc. Weinheim, 1991.

[4] A. Aceves, H. Adachihara, C. Jones, J. C. Lerman, D. W. McLaughlin, J. V. Moloney, and A. C. Newell, "Chaos and coherent structures in partial differential equations," *Physica D*, **18**, pp. 85–112, 1986.

[5] N. B. Abraham, A. M. Albano, and N. B. Tufillaro, "Complexity and chaos," in *Measures of Complexity and Chaos*, (Abraham, N.B. et als, ed.), pp. 1–27, Plenum Press, New York, 1990.

[6] J. P. Crutchfield and K. Kaneko, "Phenomenology of spatio-temporal chaos," in *Directions in chaos*, (B. L. Hao, ed.), pp. 272–353, World Scientific, Singapore, 1987.

[7] D. Z. Anderson, "Coherent optical eigenstate memory," *Opt. Lett.*, **11**, pp. 56–58, 1986, and B. H. Soffer, G. J. Dunning, Y. Owechko, and E. Marom, "Associative holographic memory with feedback using phase-conjugate mirrors, " *Opt. Lett.* , **11**, pp. 118–120, 1986.

[8] M. Brambilla, L. A. Lugiato, M. V. Pinna, F. Prati, P. Pagani, P. Vanotti, M. Y. Li, and C. O. Weiss, "The laser as nonlinear element for an optical associative memory," *Opt. Commun.*, **92**, pp. 145–164, 1992.

[9] K. P. Lo and G. Indebetouw, "Iterative image processing using a cavity with a phase conjugate mirror," *Appl. Opt.*, **31**, pp. 1745–1753, 1992.

[10] A. E. Siegman, P. A. Belanger, and A. Hardy, "Optical resonators using phase-conjugate mirrors," in *Optical Phase Conjugation*, (R. Fisher, ed.), pp. 465–535, Academic Press, New York, 1983.

[11] G. Reiner, P. Meystre and E. M. Wright, "Transverse dynamics of a phase-conjugate resonator," *J. Opt. Soc. Am.* **B 4**, pp. 675–686, 1987 and *J. Opt. Soc. Am.* **B 4**, pp. 865–874, 1987; G. Reiner, M. R. Belic and P. Meystre, "Optical turbulence in phase-conjugate resonators," *J. Opt. Soc. Am* **B 5**, pp. 1193–1210, 1988.

[12] G. Indebetouw and S. R. Liu, "Defect-mediated spatial complexity and chaos in a phase-conjugate resonator," *Opt. Commun.*, **91**, pp. 321–330, 1992.

[13] S. R. Liu and G. Indebetouw, "Periodic and chaotic spatiotemporal states in a phase-conjugate resonator using a photorefractive $BaTiO_3$ phase-conjugate mirror," *J. Opt. Soc. Am.*, **B 9**, pp. 1507–1520, 1992.

[14] P. Coullet and J. Lega, "Defect-mediated turbulence in wave patterns," *Europhys. Letters*, **7**, pp. 511–516, 1988 and P. Coullet, L. Gil, and J. Lega, "Defect-mediated turbulence, " *Phys. Rev. Lett.*, **62**, pp. 1619–1622, 1989.

[15] M. Brambilla, F. Battipede, L. A. Lugiato, V. Penna, F. Prati, C. Tamm, and C. O. Weiss, "Transverse laser patterns. II. Variational principle for pattern selection, spatial multistability and laser hydrodynamics," *Phys. Rev. A*, **43**, pp. 5113–5120, 1991.

[16] F. T. Arecchi, "Space-time chaos in optical media: Dry-hydrodynamics," in *ECOOSA 90–Quantum optics*, (M. Bertolotti and E. R. Pike, eds.), Institute of Physics,Bristol, 1990.

[17] F. T. Arecchi, G. Giacomelli, P. L. Ramazza, and S. Residori, "Vortices and defect statistics in two-dimensional optical chaos," *Phys. Rev. Lett.*, **67**, pp. 3749–3752, 1991.

[18] V. L. Vinetskii, N. V. Kukhtarev, S. G. Odulov, and M. S. Soskin, "Dynamic self-diffraction of coherent light beams," *Sov. Phys. Usp*, **22**, pp. 742–756, 1979; and N. V. Kukhtarev, V. B. Markov, S. G. Odulov, M. S. Soskin, and V. L. vinetskii, "Holographic storage in electro-optic crystal. II. Beam coupling-light-amplication," *Ferroelectrics*, **22**, pp. 961–964, 1979.

[19] A. C. Newell, "The dynamics of patterns: A survey," in *Propagation in systems far from equilibrium*, (J. W. Wesfried et. als., ed.), pp. 122–155, Springer-Verlag, Berlin, 1988.

[20] G. D'Alessandro and G. L. Oppo, "Gauss-Laguerre modes: a "sensible" basis for laser dynamics," *Opt. Commun.*, **88**, pp. 130–136, 1992.

[21] A. E. Siegman, *Laser.* University Science Book, Mill Valey, 1986.

[22] V. Kalinin and L. Solymar, "Transient effects in four-wave mixing in photorefractive passive phase conjugate mirrors," *Applied Physics*, **B 45**, pp. 129–135, 1988.

[23] W. Krolikowski, B. S. Chen, and M. Cronin-Golomb, "Temporal instabilities in an externally driven ring phase conjugator," *J. Opt. Soc. Am.*, **B 8**, pp. 1455–1460, 1991.

Figure Captions

Figure 1: Sketch of the phase-conjugate resonator. PCM, phase-conjugate mirror (externally pumped photorefractive crystal); M, planar mirror; H_1, H_2, apertures controlling the Fresnel number of the afocal cavity.

Figure 2: Sections of time series of the local intensity fluctuations at the output of the PCM for different values of the off-Bragg parameter *bd* (numerical simulation).

Figure 3: Bifurcation diagram of the local intensity fluctuations at the output of the PCM with the off-Bragg parameter as control parameter (numerical simulation).

Figure 4: Power spectra of the time series of fig. 2 showing a variety of motions: (a)periodic, (b,c)quasiperiodic with two incommensurate frequencies, (d)chaotic , and (e)frequency locked at period 13.

Figure 5: Phase space portraits corresponding to the motions illustrated in figs 2, 4 showing (a)a limit cycle, (b,c)broadened tori, (d)a diffuse torus, (e)a 13-loop trajectory.

Figure 6: Snapshot of the field magnitude distribution $|A_4|$ at the output of the PCM for $bd = -2.45$, showing four dark spots identified as four vortices in fig. 7 (numerical simulation).

Figure 7: Phase contours of the wavefront at the output of the PCM revealing the presence of two pairs of vortices of opposite charges.

Figure 8: Temporal evolution of the field magnitude at the output of the PCM along the line $x = 0.75$ beam waist for the same off-Bragg parameter values as used in fig. 2, 4, 5. (a)single frequency periodic oscillation, (b)quasiperiodic oscillations with incommensurate transverse modulation, (c)similar to b but with deeper modulation (note the time scale change), (d)irregular transverse modulation leading to chaos, (e)frequency locked oscillations(period 13) with transverse modulation commensurate with the main frequency.

Figure 9: Spatial correlation index distribution with respect to the fluctuations at the origin for $bd = -2.3$. No defects nucleates in the beam, but the amplitude and phase breathe periodically.

Figure 10: Interferogram snapshots of the wavefront at the output of the PCM at $bd = -2.45$ showing the nucleation, motion and annihilation of two pairs of vortices of opposite charges.

Figure 11: (a)Distribution of the vortices' positions at $bd = -2.45$ showing trajectories confined to well defined area. (b)Corresponding spatial correlation index distribution with respect to the intensity fluctuation at the origin.

Figure 12: Same as fig. 11 at $bd = -2.55$.

Figure 13: (a)Distribution of the vortices' position at $bd = -2.75$ (chaotic motion) showing trajectories randomly visiting large area. (b)Corresponding spatial correlation index distribution with respect to the intensity fluctuations at the origin. (c) same as b but with respect to the intensity fluctuations at a point (x=1, y=0.3) frequently visited by a vortex.

Figure 14: Interferogram snapshots of the wavefront at the output of the PCM for $bd = -3.18$. No defect nucleates but the phase breathes periodically in two concentric annular area.

Figure 15: Spatial correlation index distribution with respect to the intensity fluctuations at the origin for $bd = -3.18$.

Figure 16: Interferogram snapshot at the output of the PCM revealing the presence of two pairs of vortices of opposite charges. (experimental result)

Figure 17: Sections of experimental time series of the local intensity fluctuations at the output of the PCM for different relative values of the off-Bragg parameter. (experimental results)

Figure 18: Power spectra of the time series of fig. 17 showing a variety of motions: (a)periodic, (b)chaotic, (c)frequency locked (period 3), (d,e)quasiperiodic.

Figure 19: Delayed time phase space portraits of the local intensity fluctuations of fig. 17, 19 showing (a)a noisy limit cycle, (b)a featureless portrait, (c)a period three limit cycle and (d)a diffuse portrait possibly representing a quasiperiodic motion (experimental results).

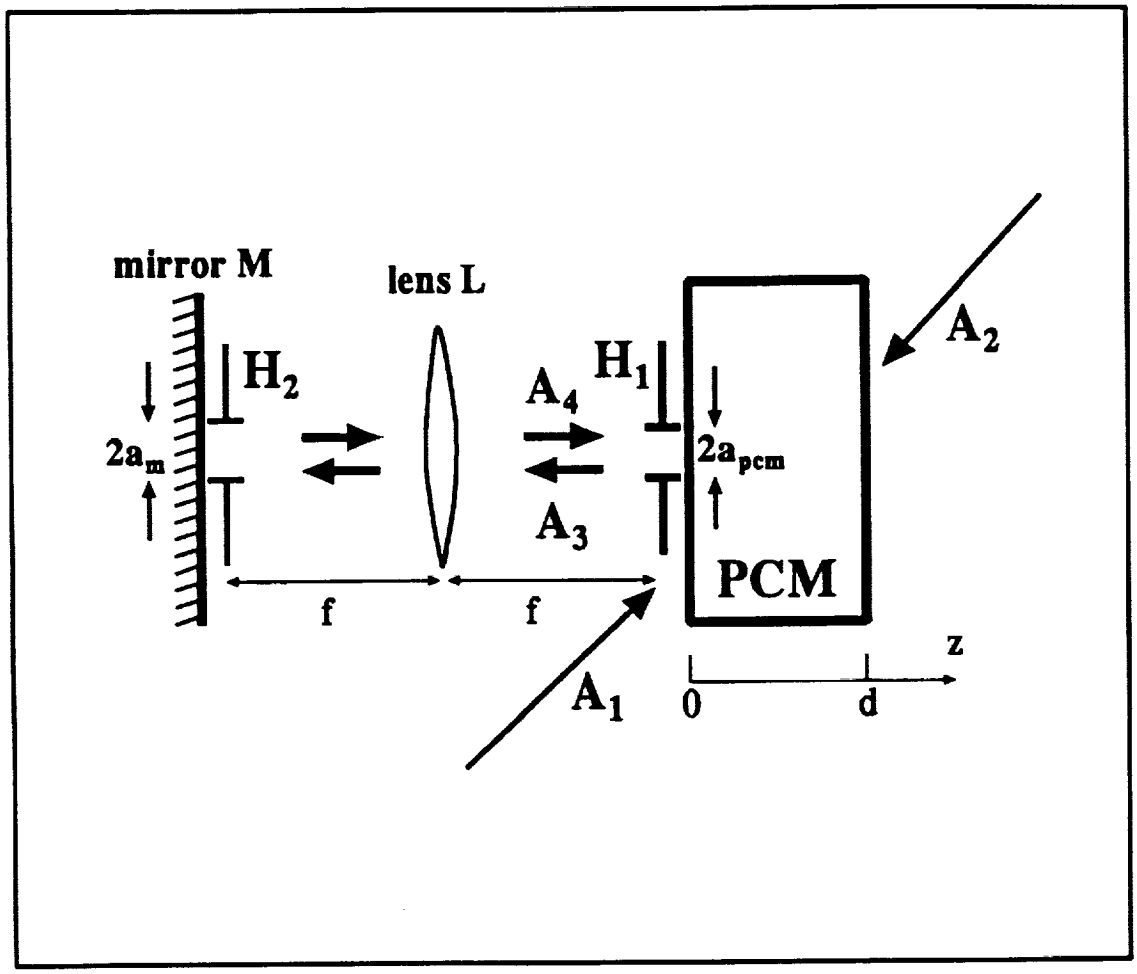

Liu - Indebetouw Fig. 1

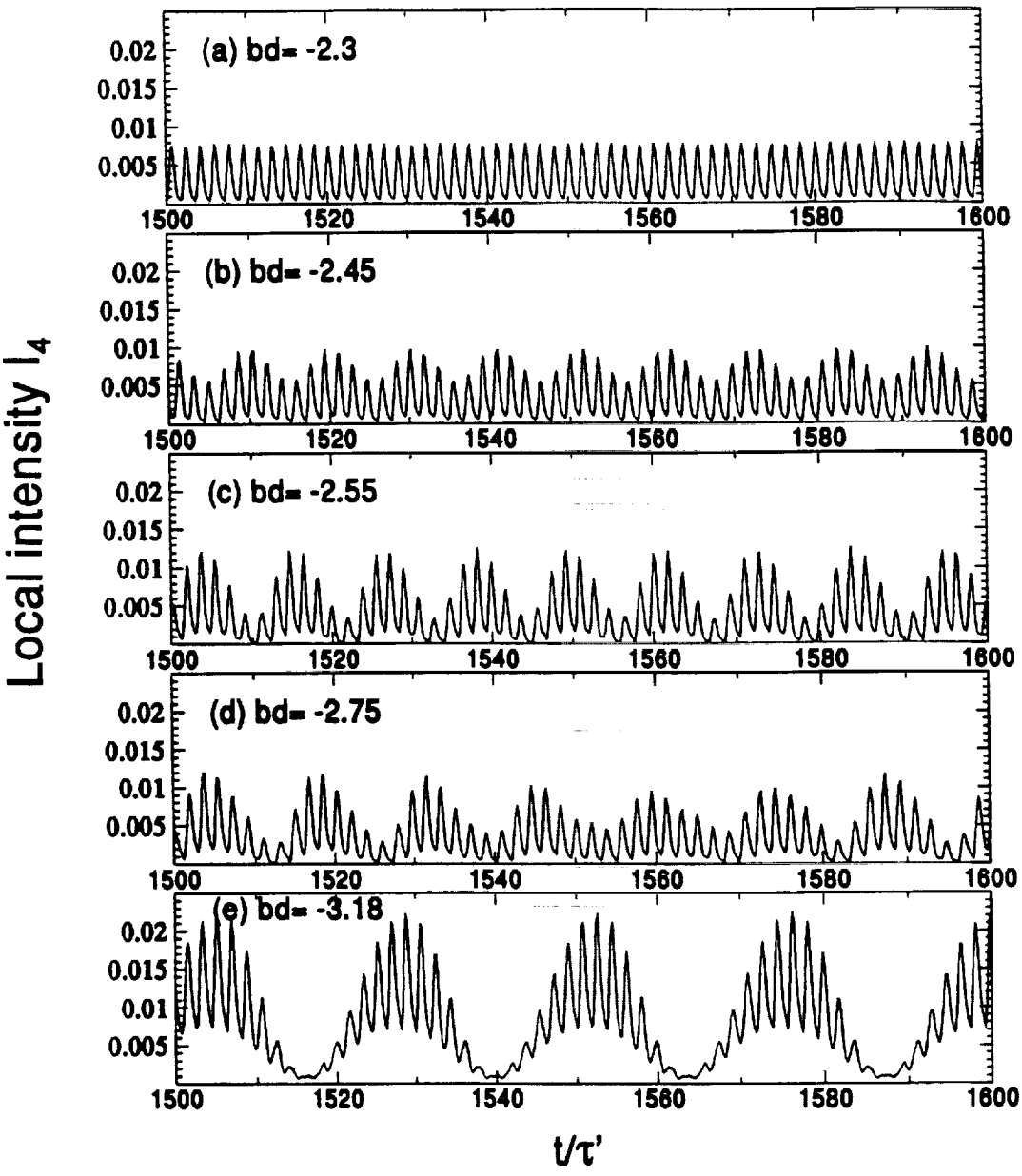

Liu/Indebetouw Fig. 2

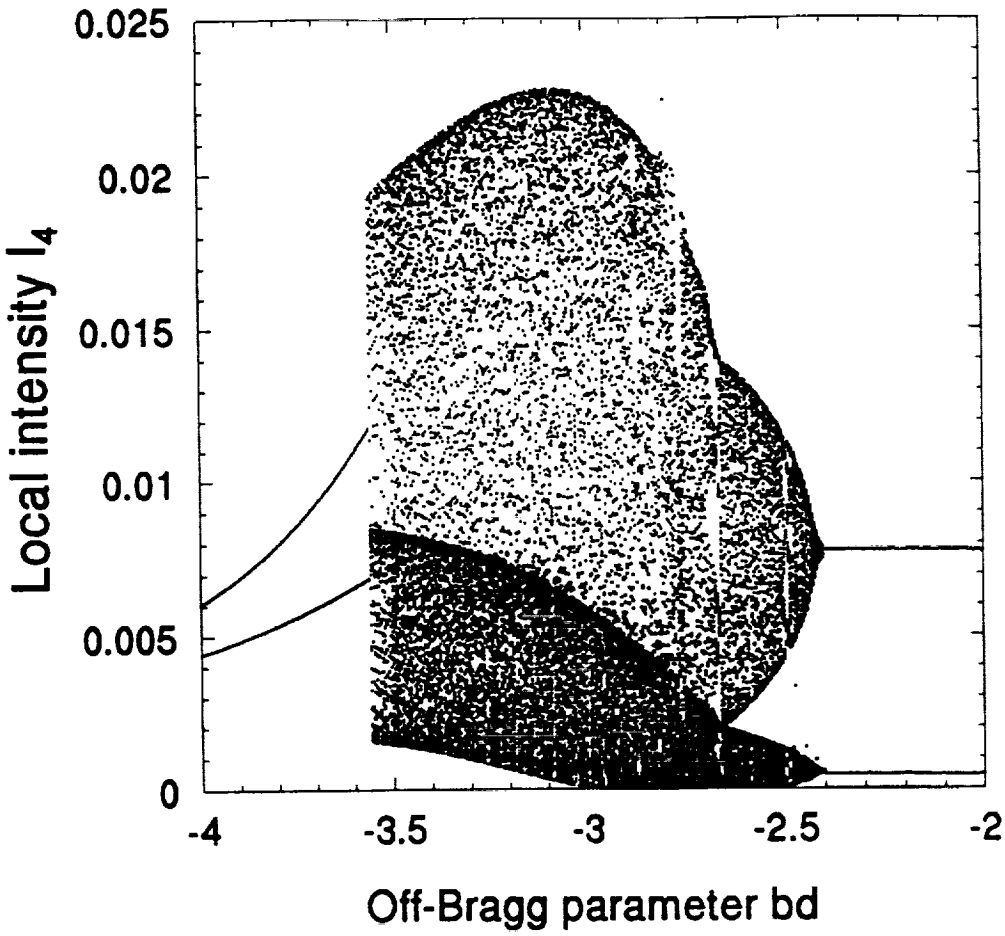

Liu/Indebetouw Fig. 3

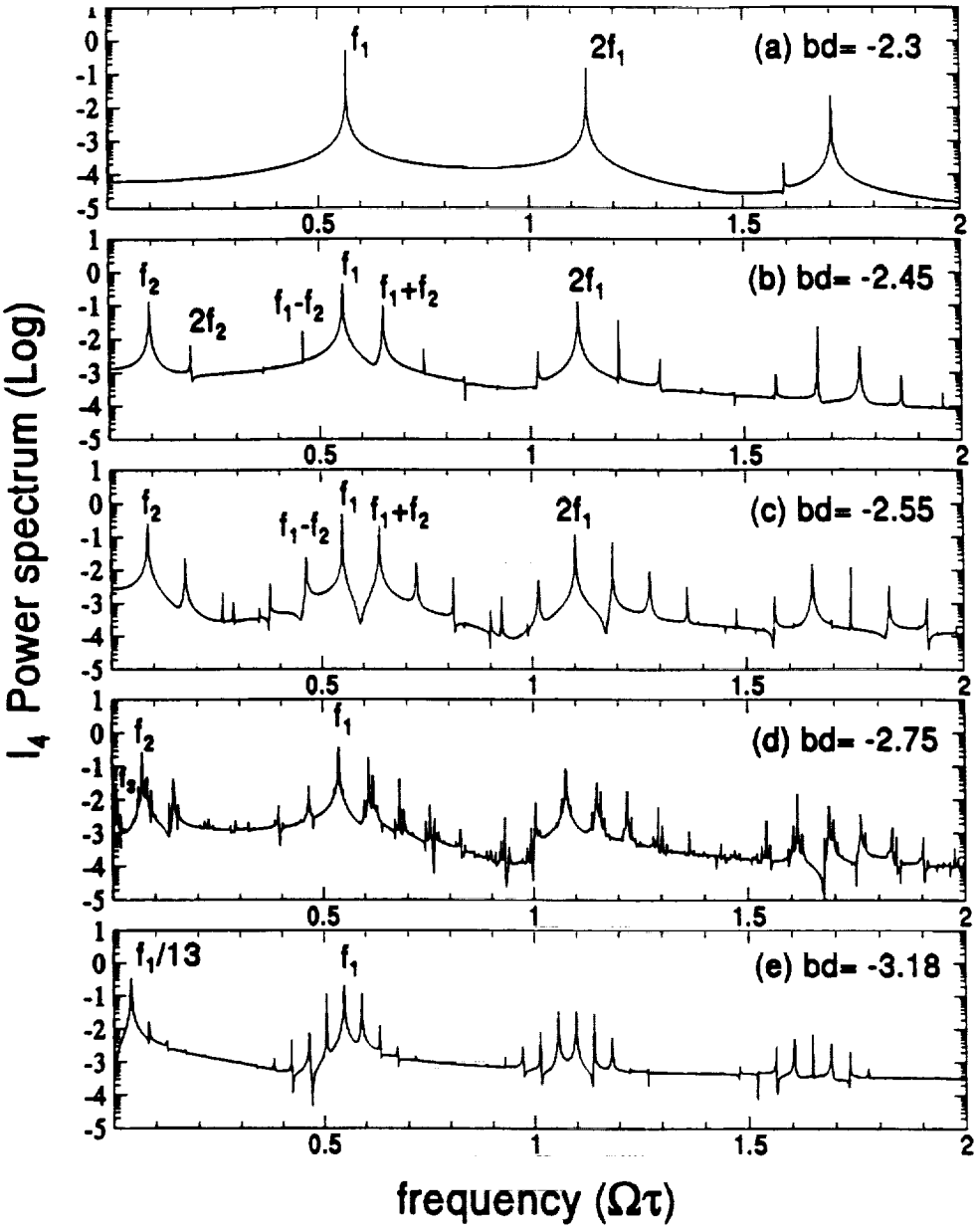

Liu/Indebetouw Fig. 4

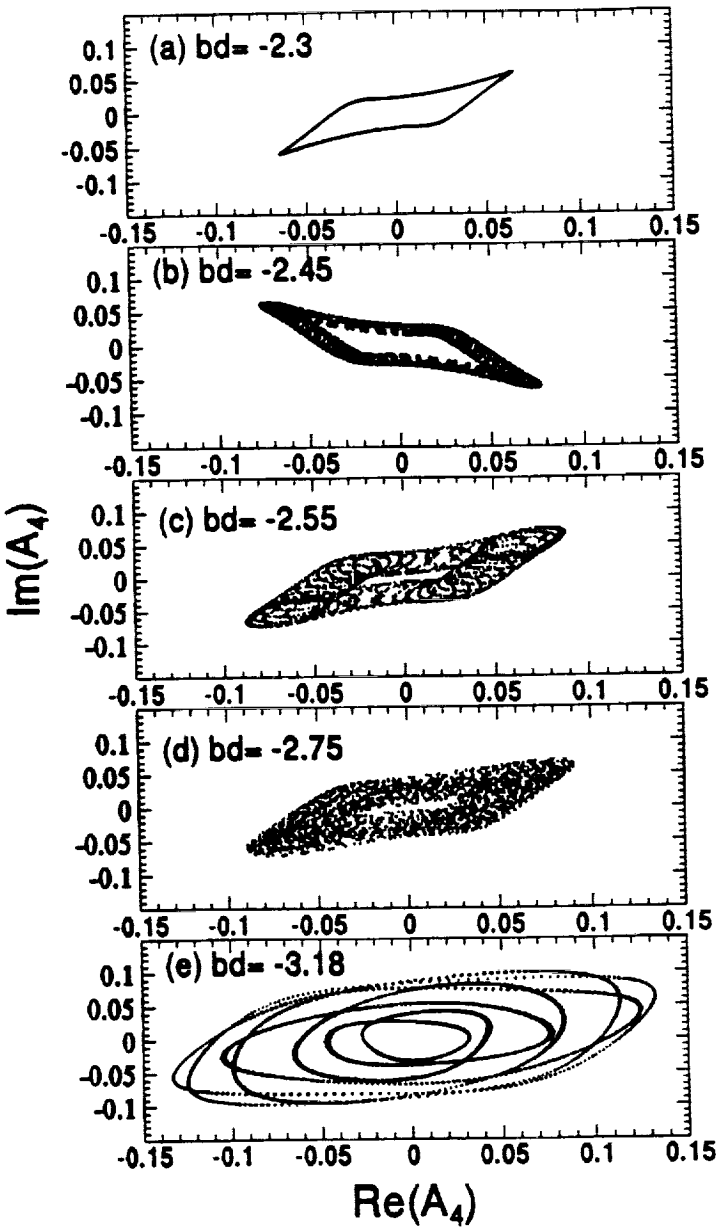

Liu / Indebetouw Fig. 5

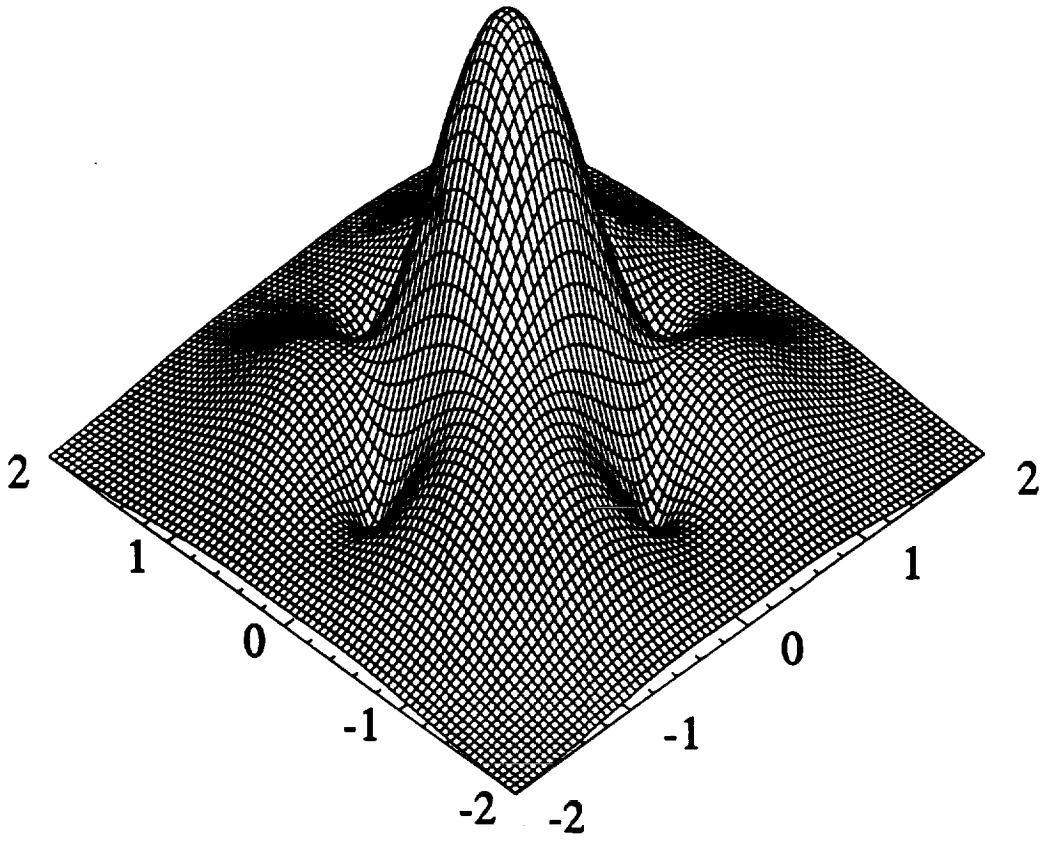

bd= -2.45, t=1502.8τ'

Liu / Indebetouw Fig. 6

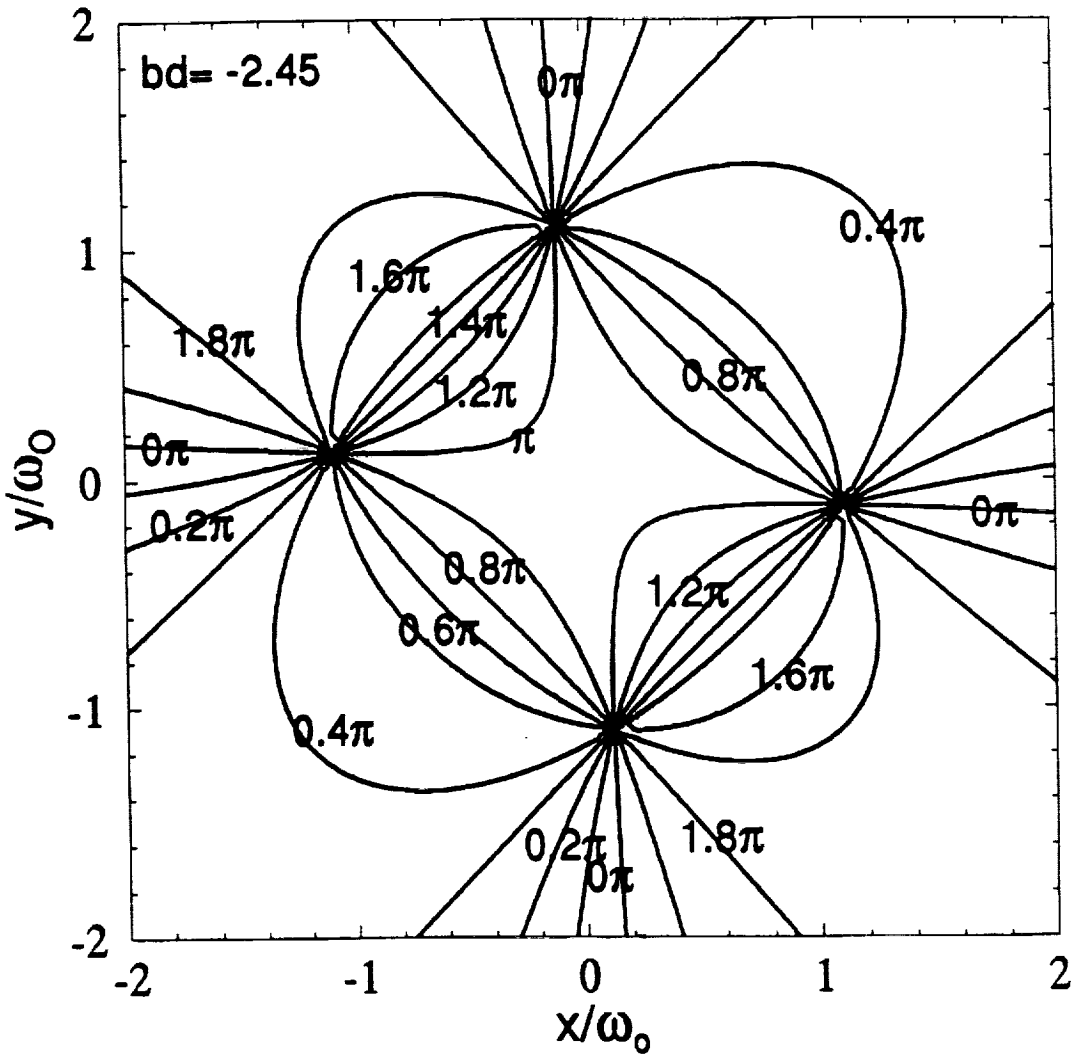

Liu/Indebetouw Fig. 7

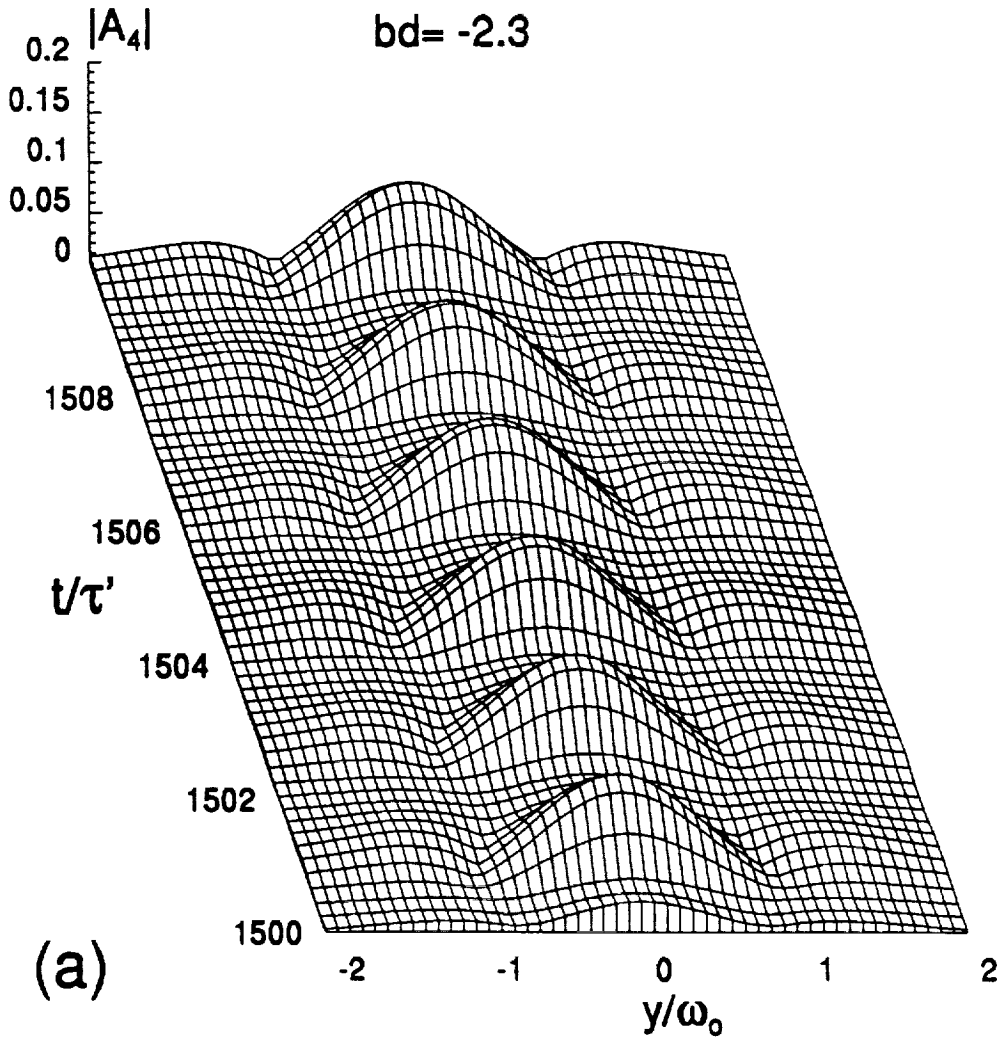

Liu/Indebetouw Fig. 8a

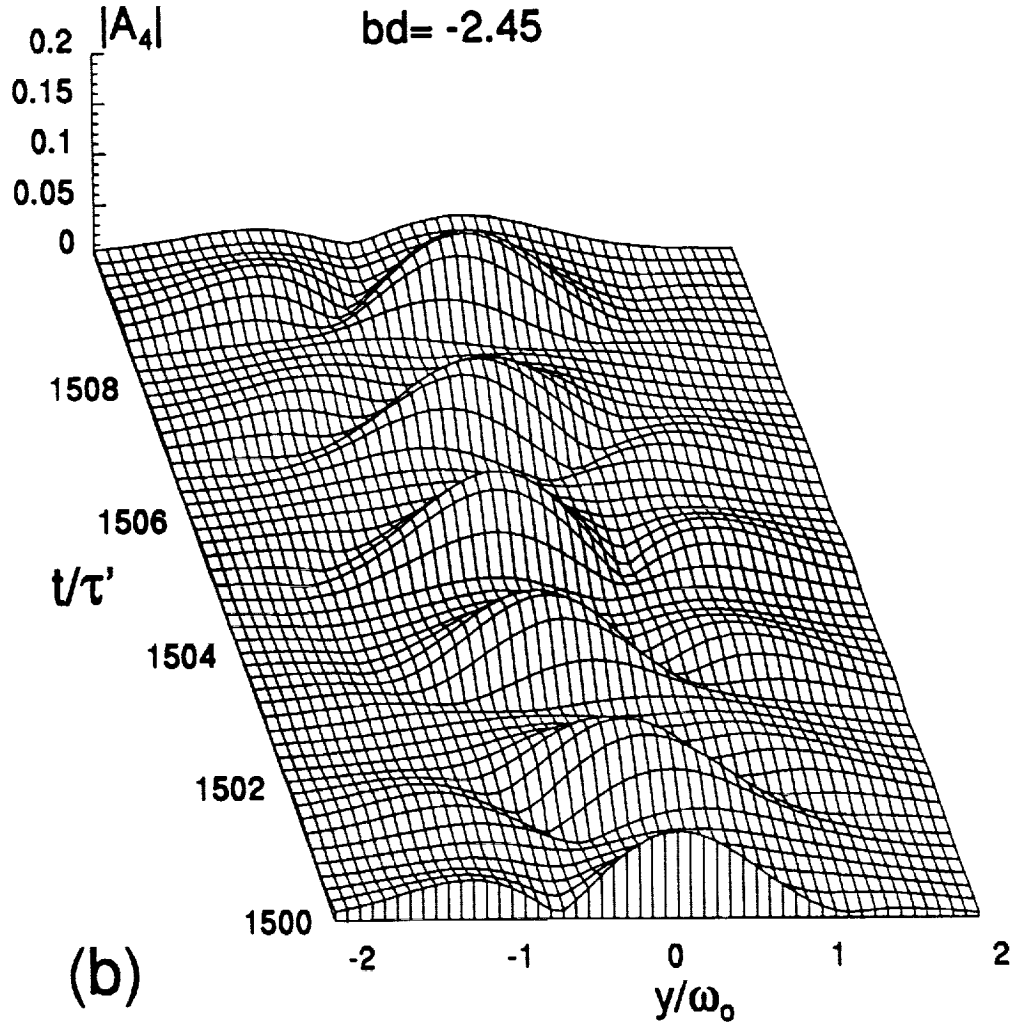

Liu / Indebetouw Fig. 8b

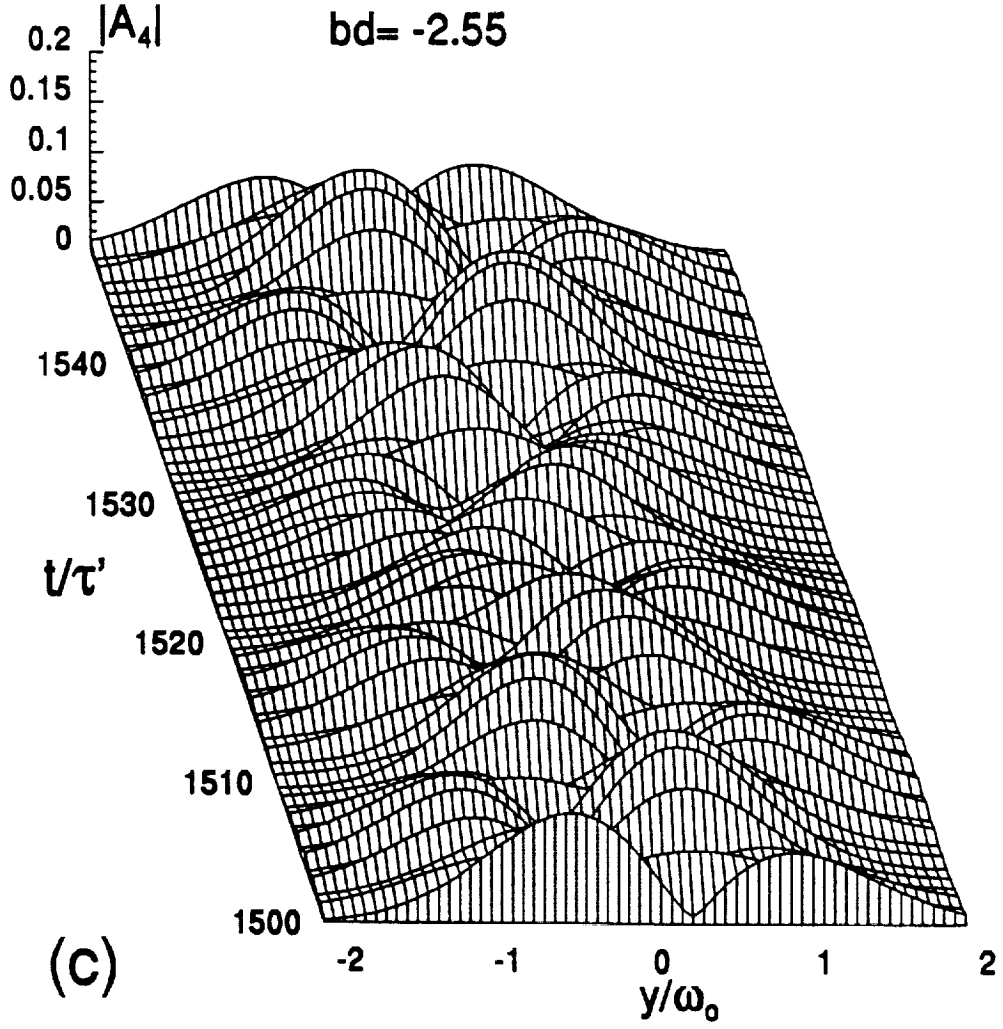

Liu / Indebetouw Fig. 8C

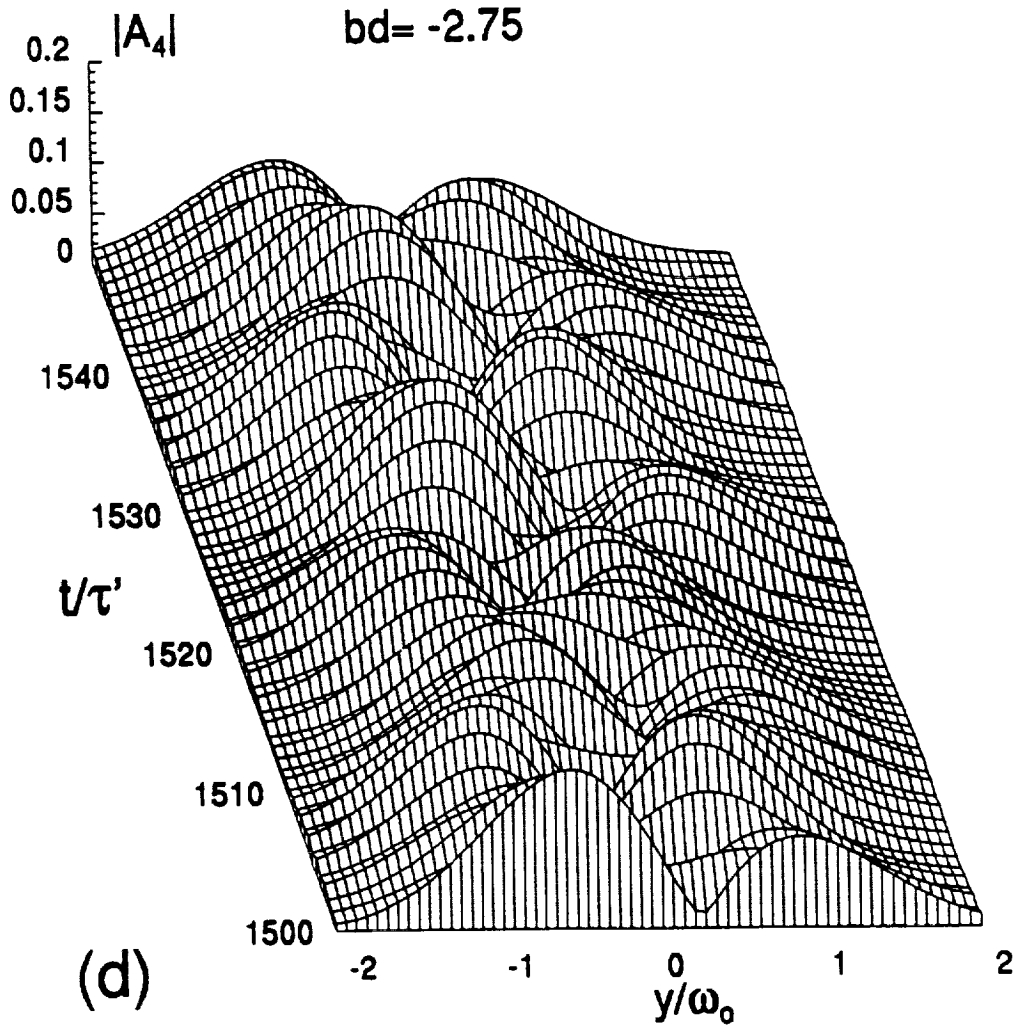

Liu / Inadebetouw Fig. 8d

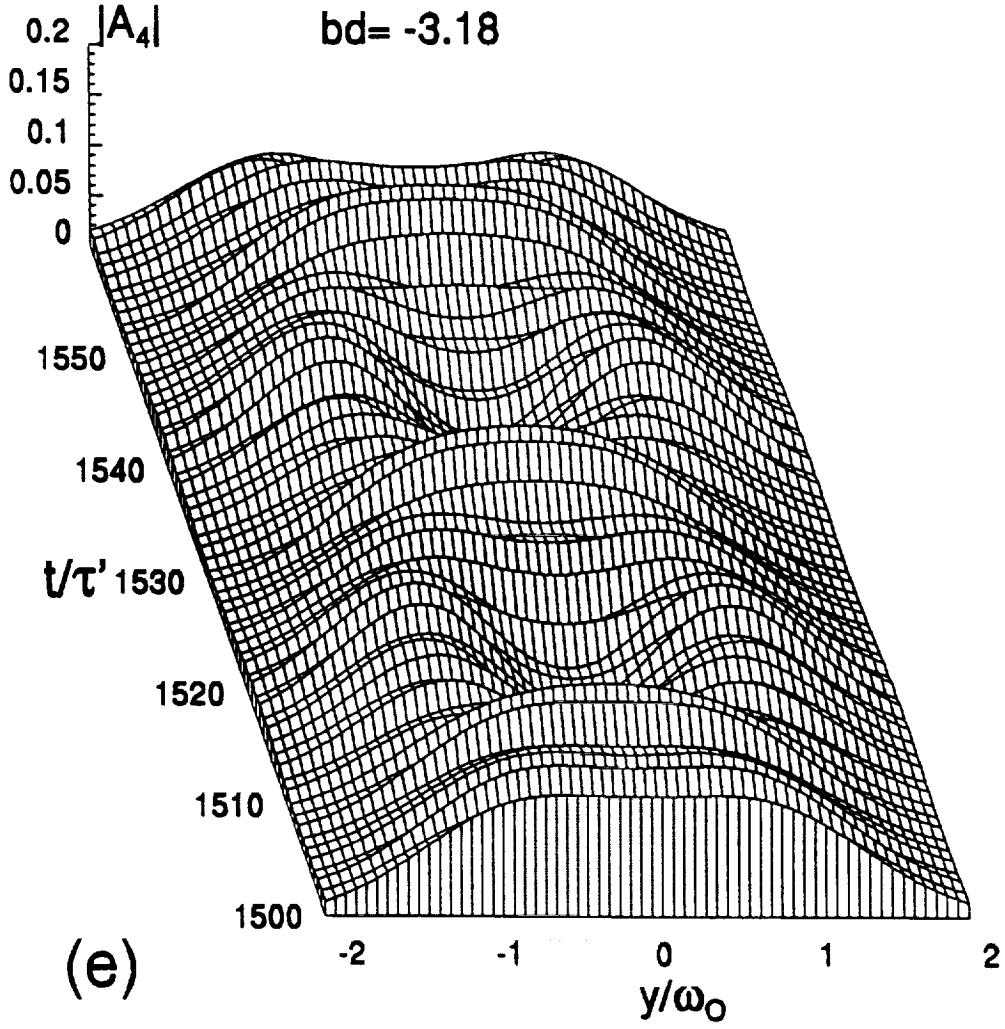

Liu/Indebetouw Fig. 8e

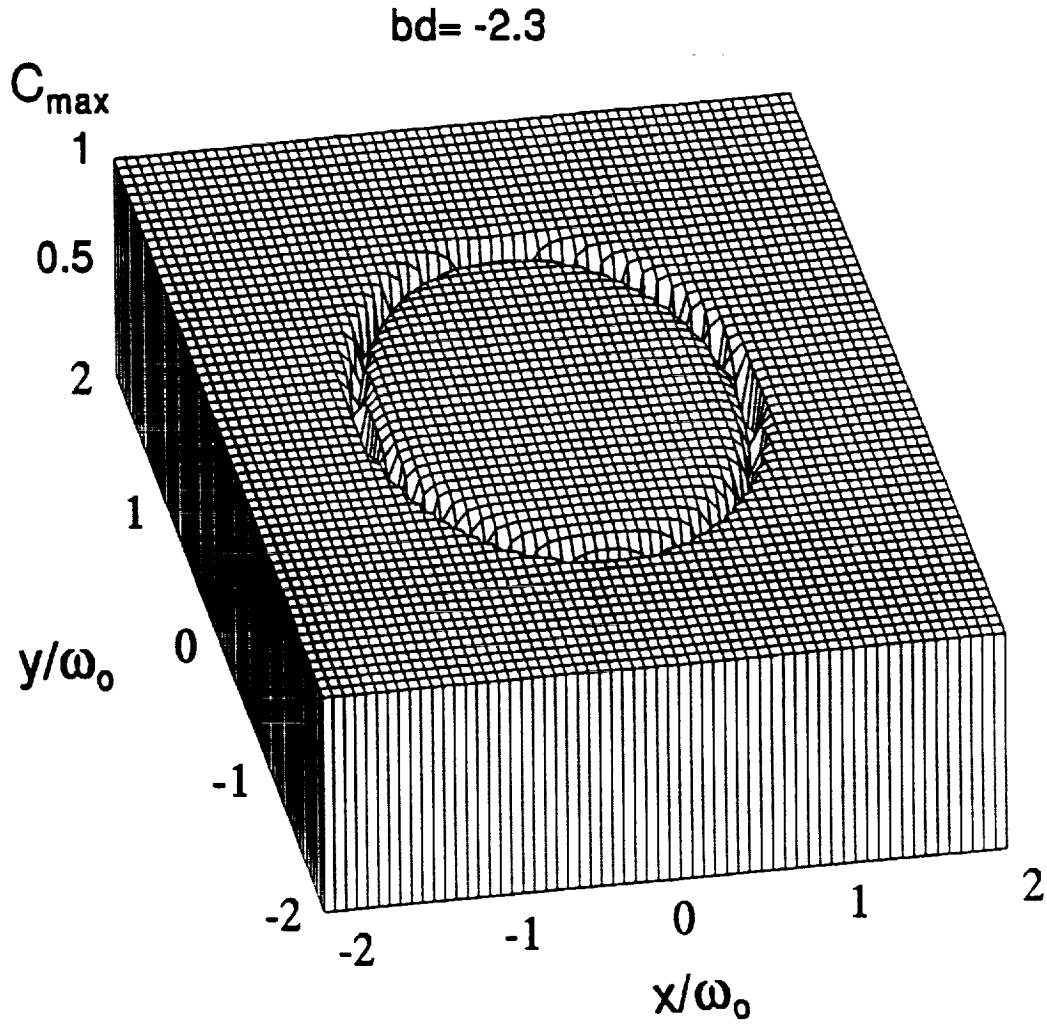

Liu/Indebetouw Fig. 9

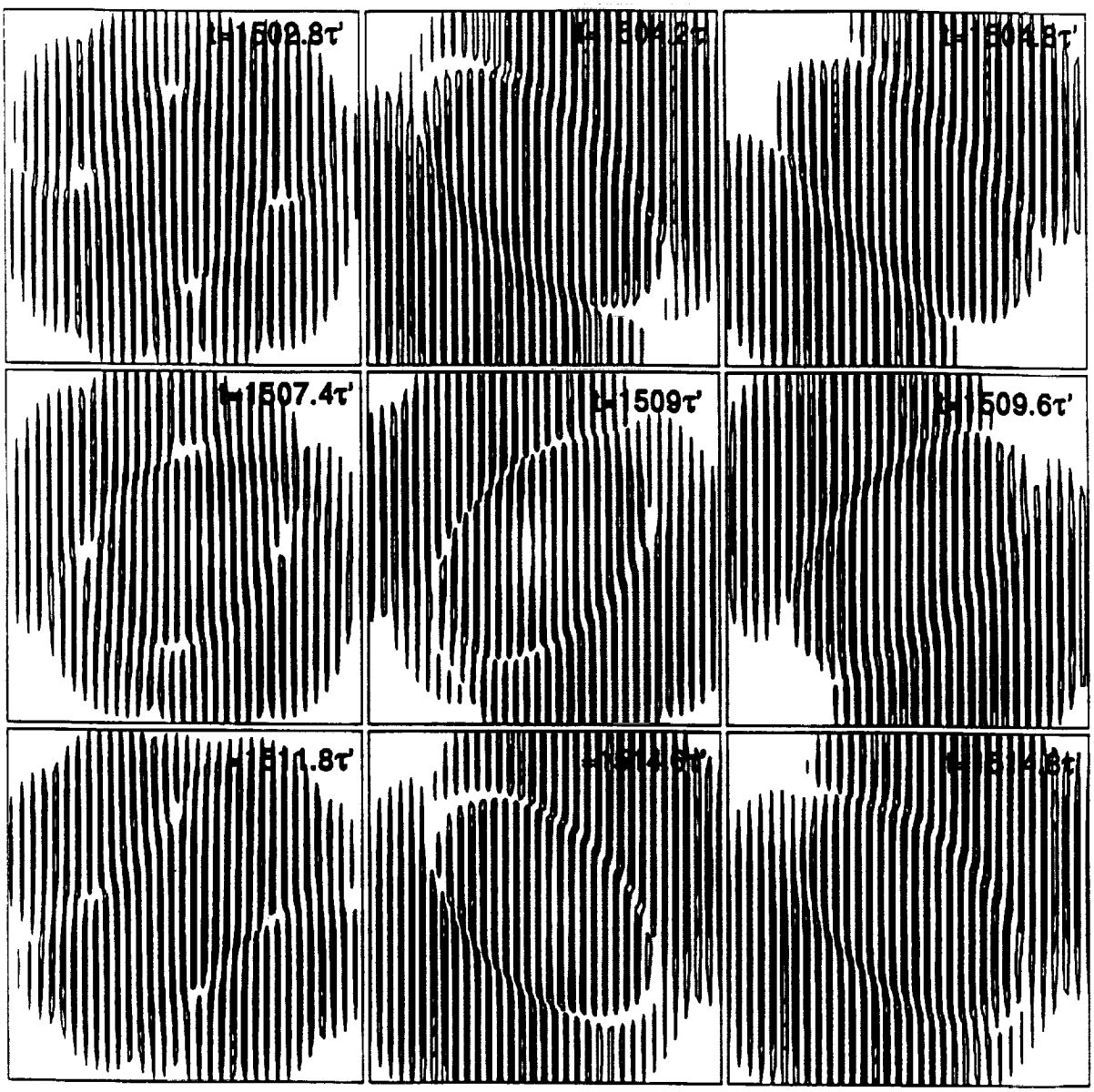

Liu / Indebetouw Fig. 10

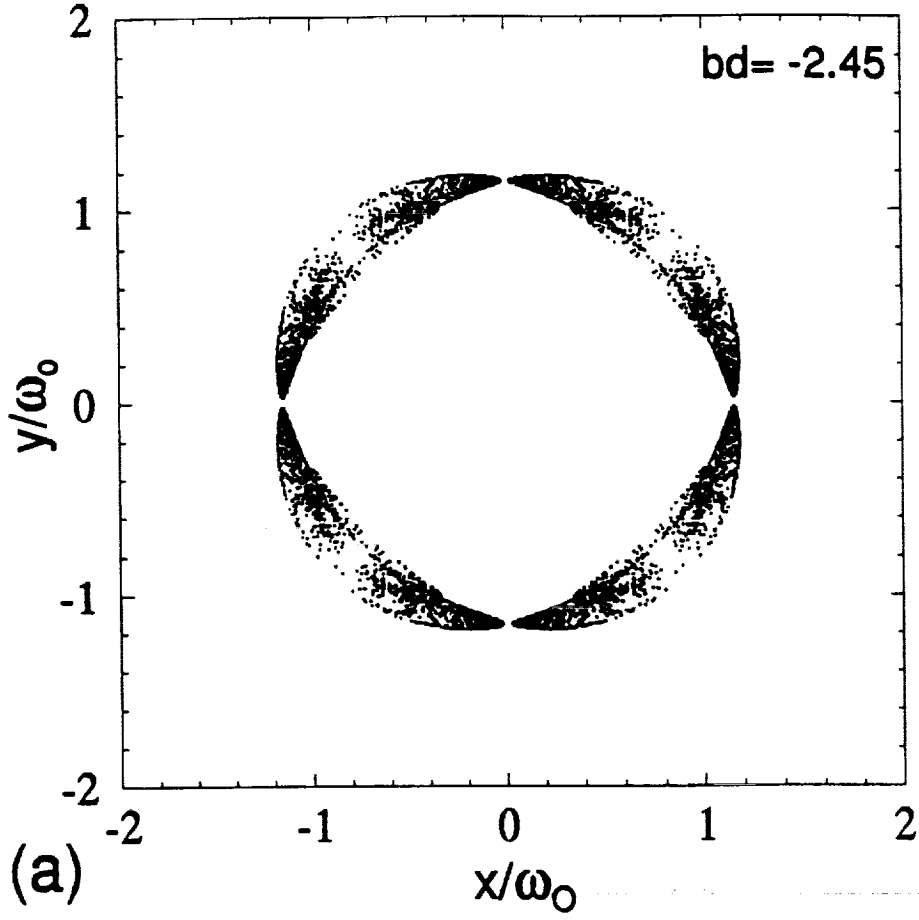

Liu/Indebetouw Fig. 11a

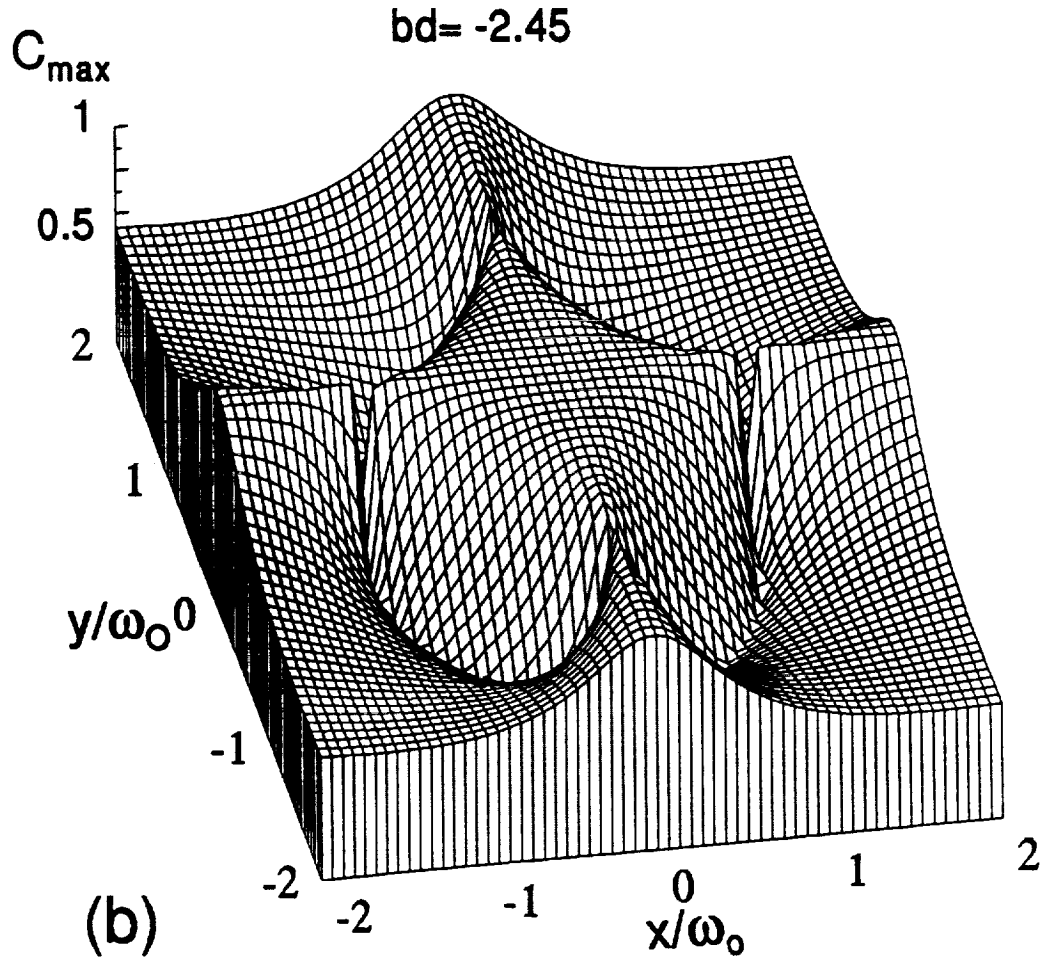

Liu / Indebetouw Fig. 11b

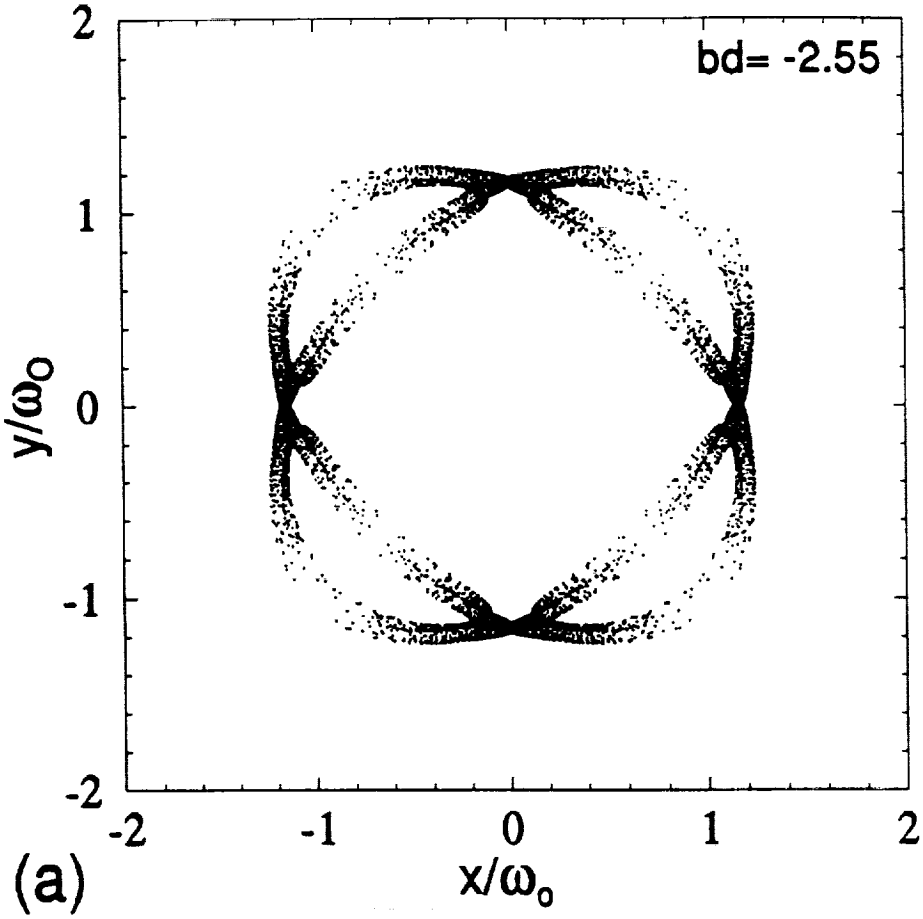

Liu/Indebetouw Fig. 12a

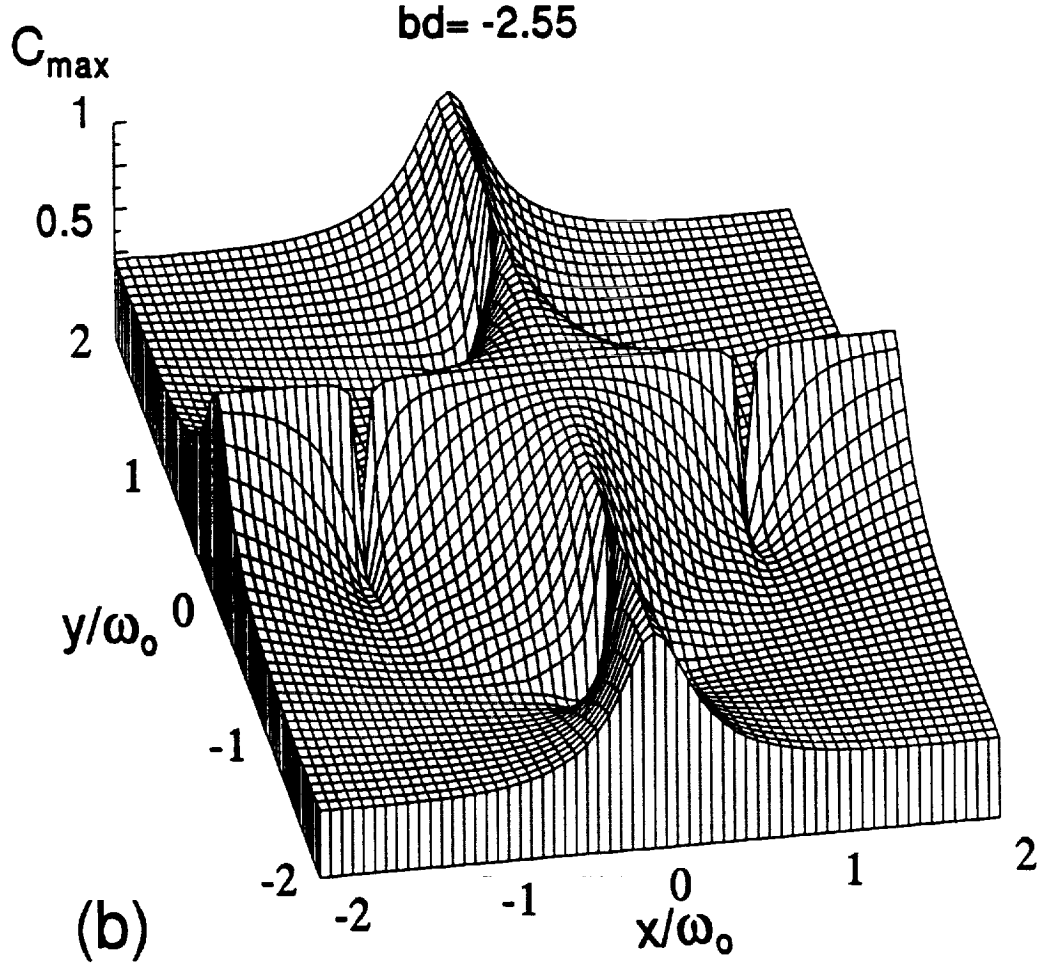

Liu | Indebetouw Fig. 12b

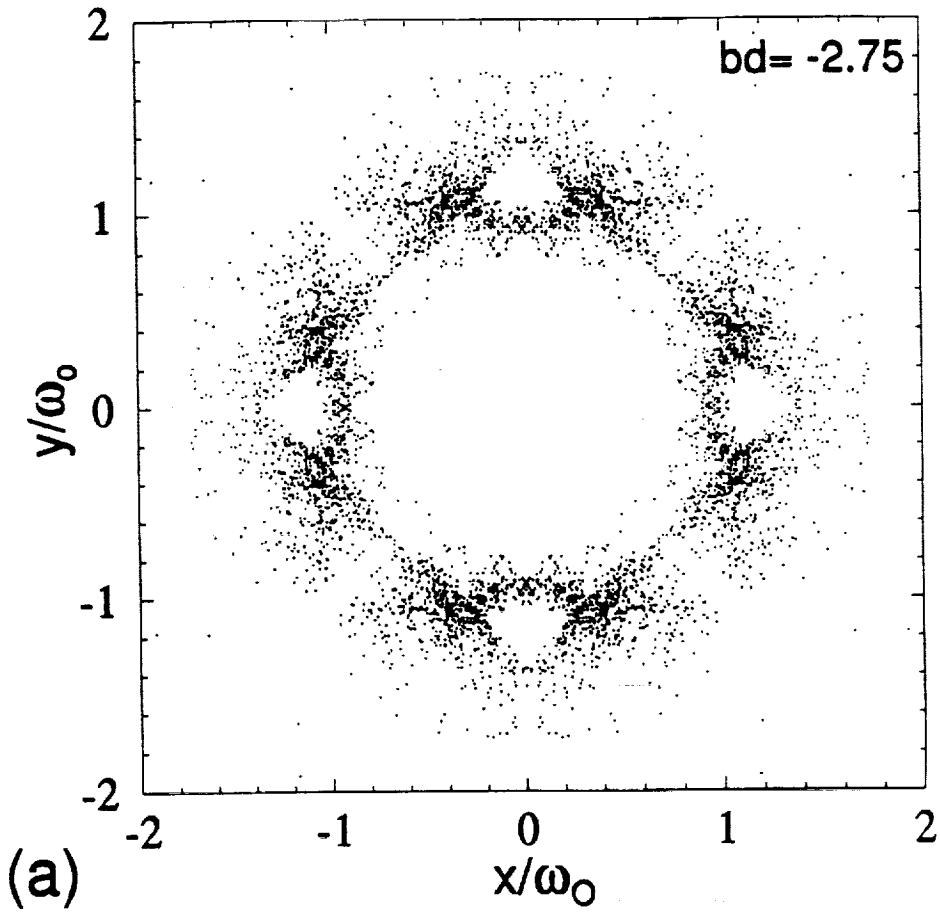

Liu/ Indebetouw Fig. 13a

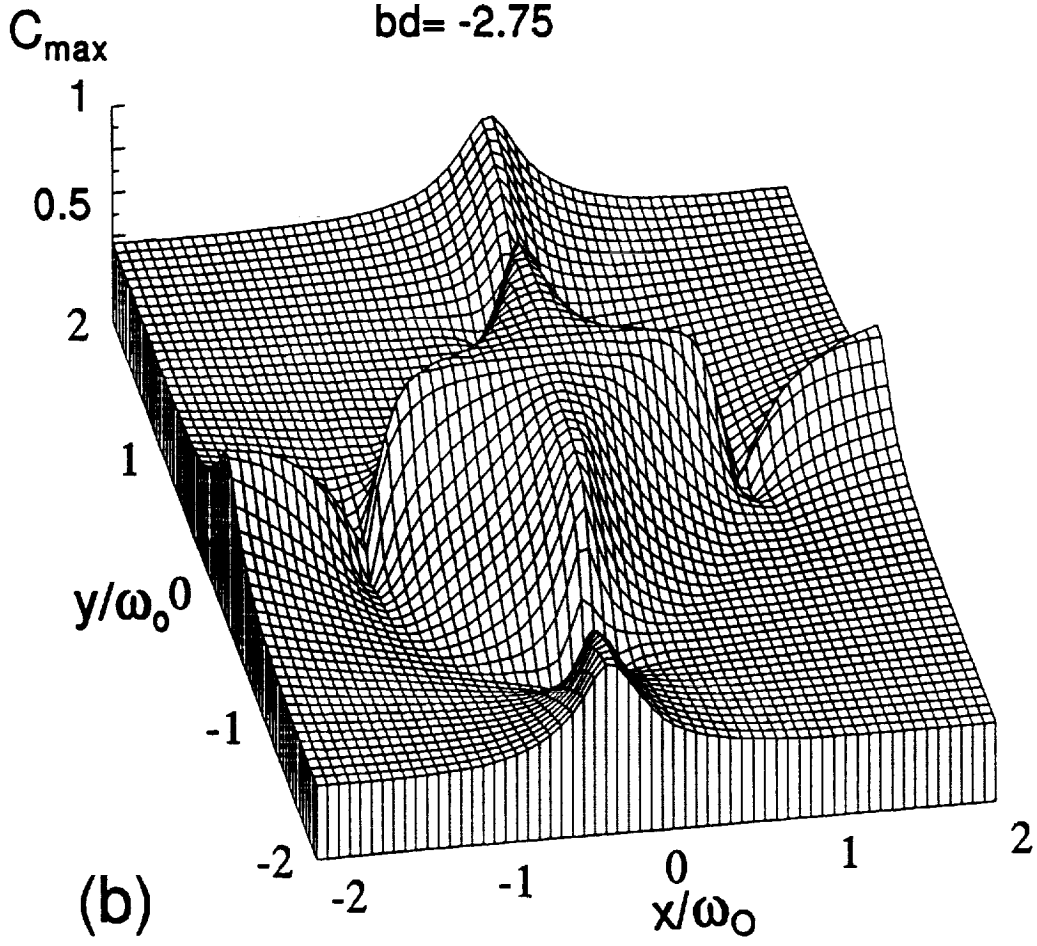

Liu/Indebetouw Fig. 13b

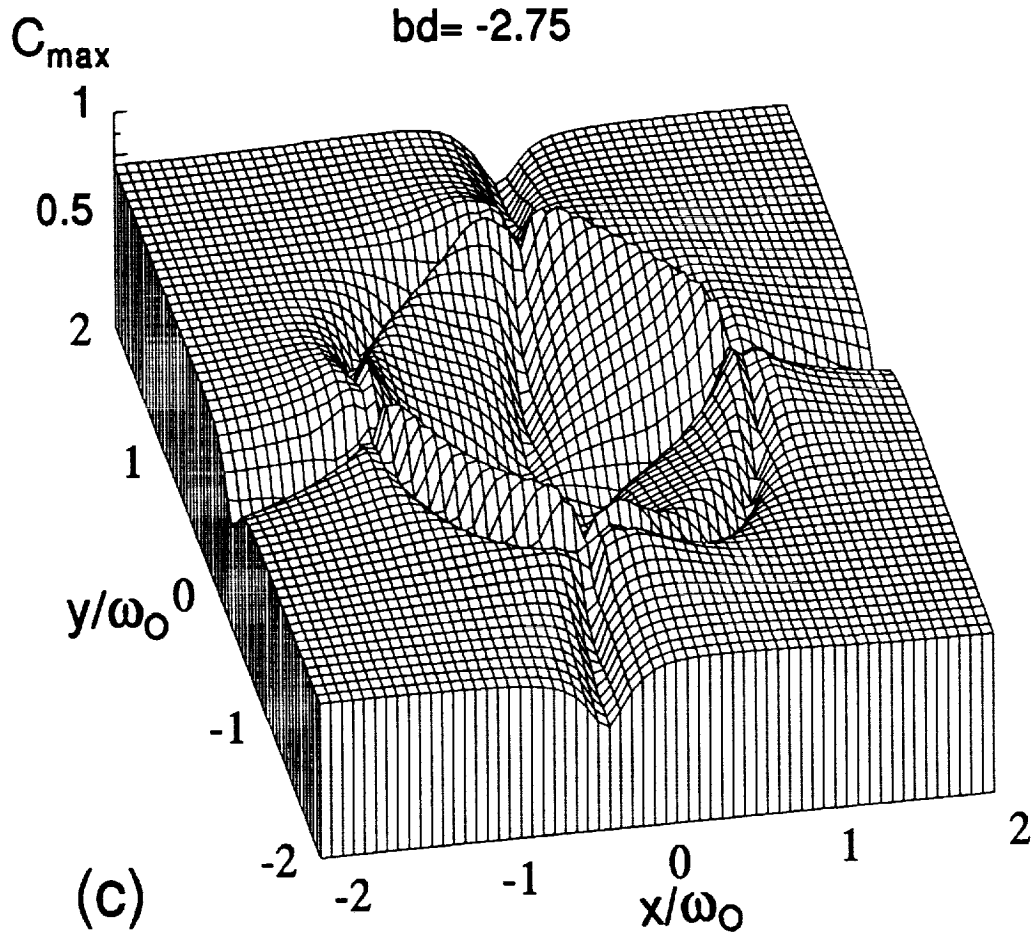

Liu | Indebetouw Fig. 13c

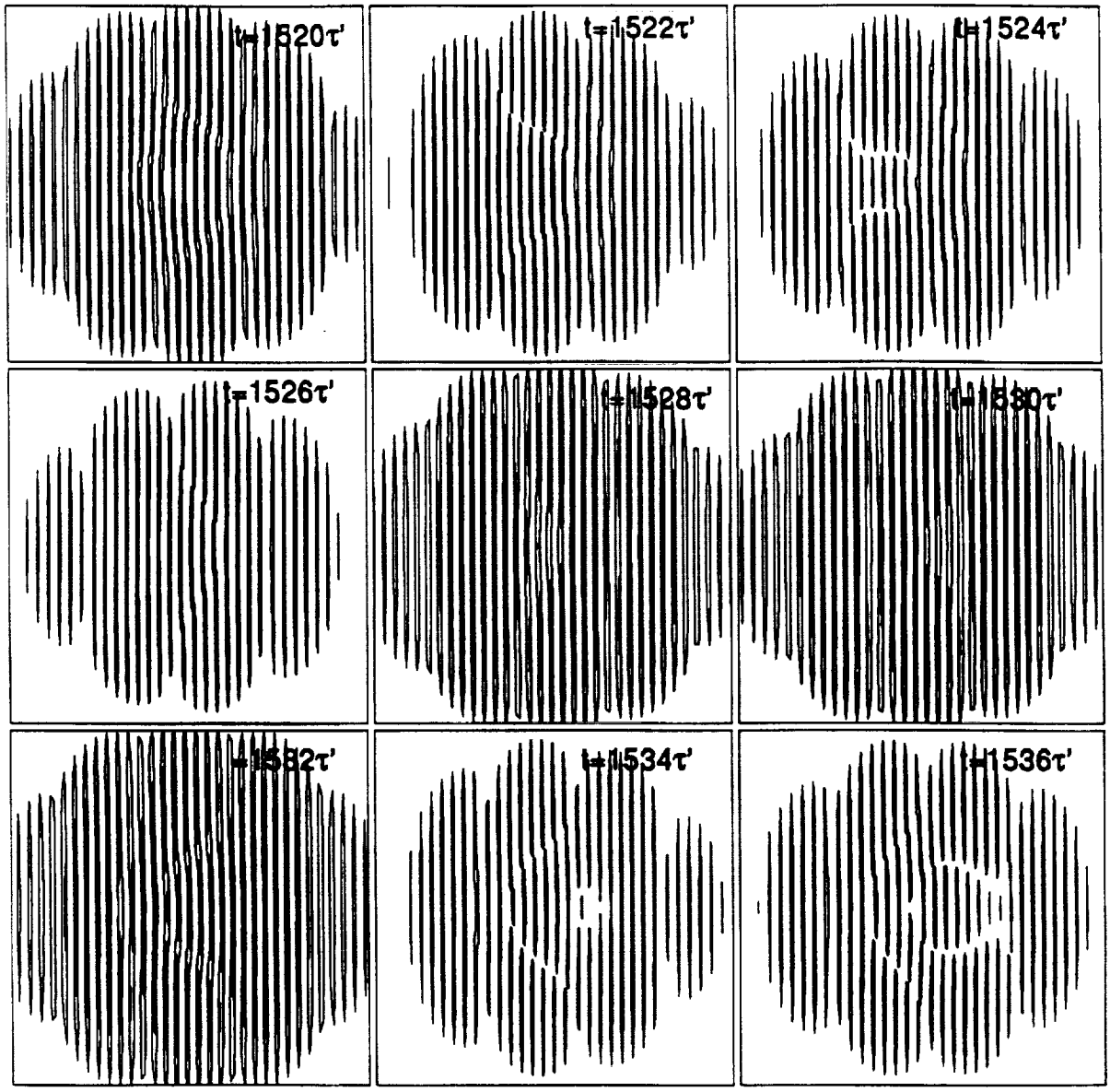

Liu/Indebetouw Fig. 14

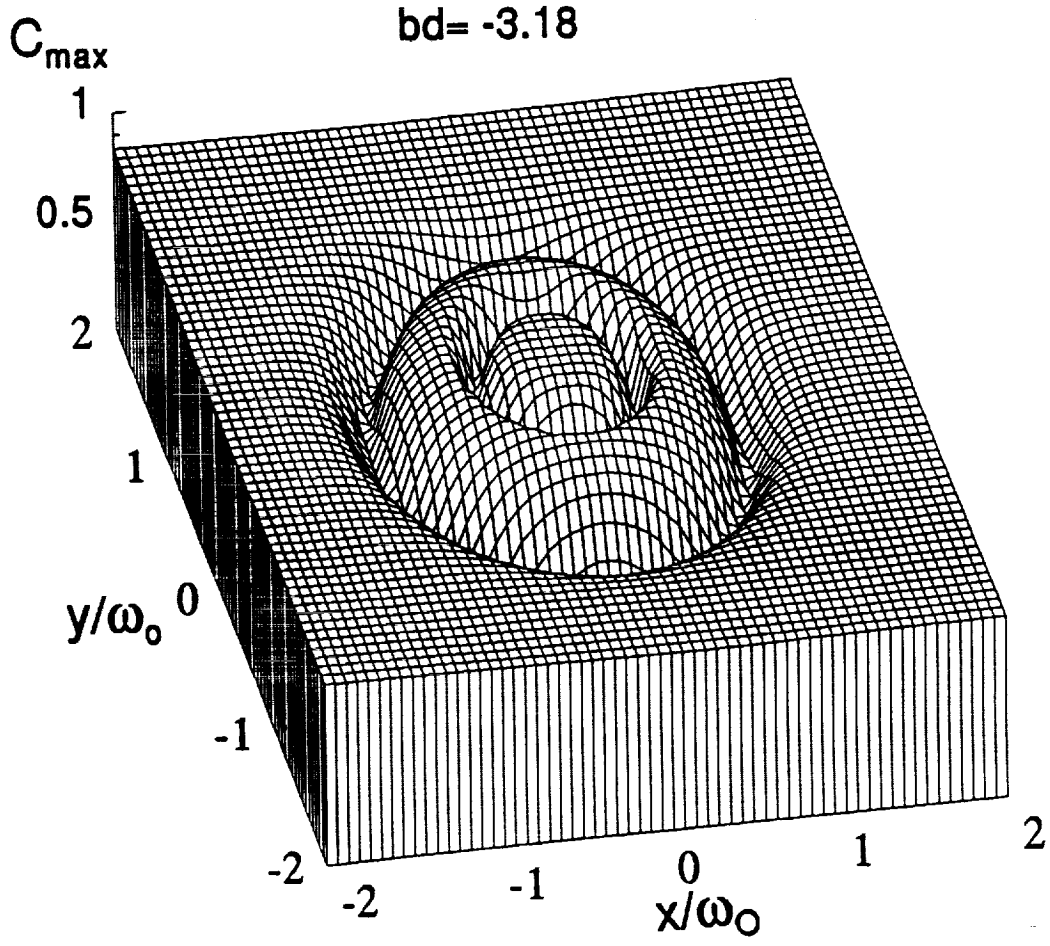

Liu-Indebetouw Fig. 15

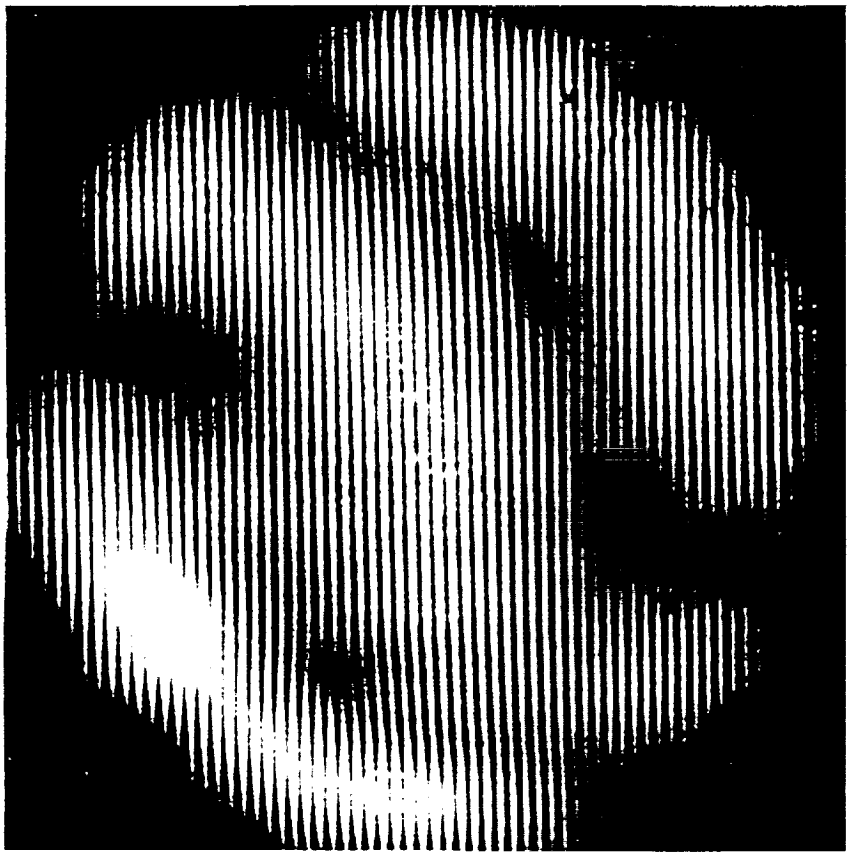

Liu/Indebetouw Fig. 16

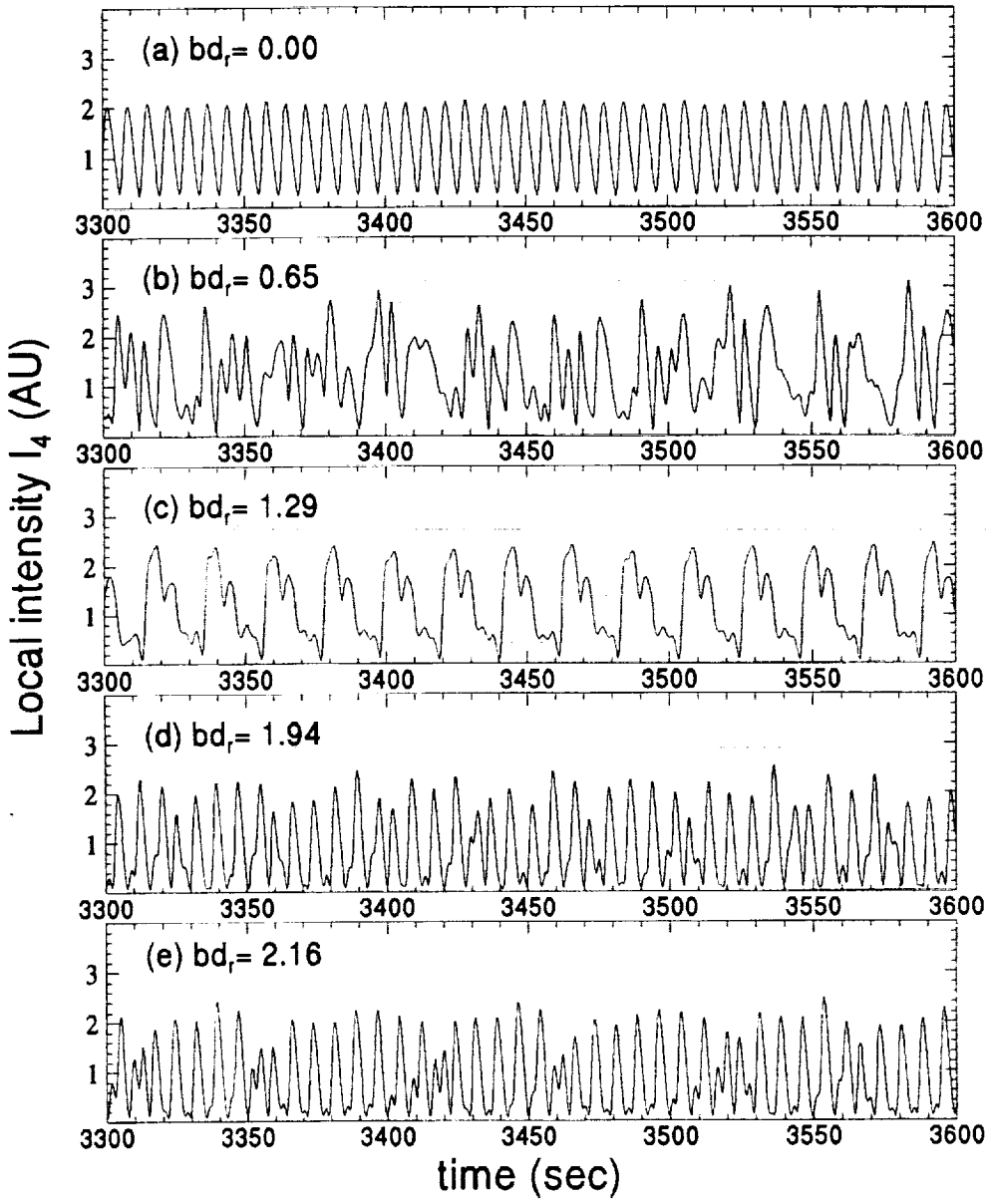

Liu / Indebetouw Fig. 17

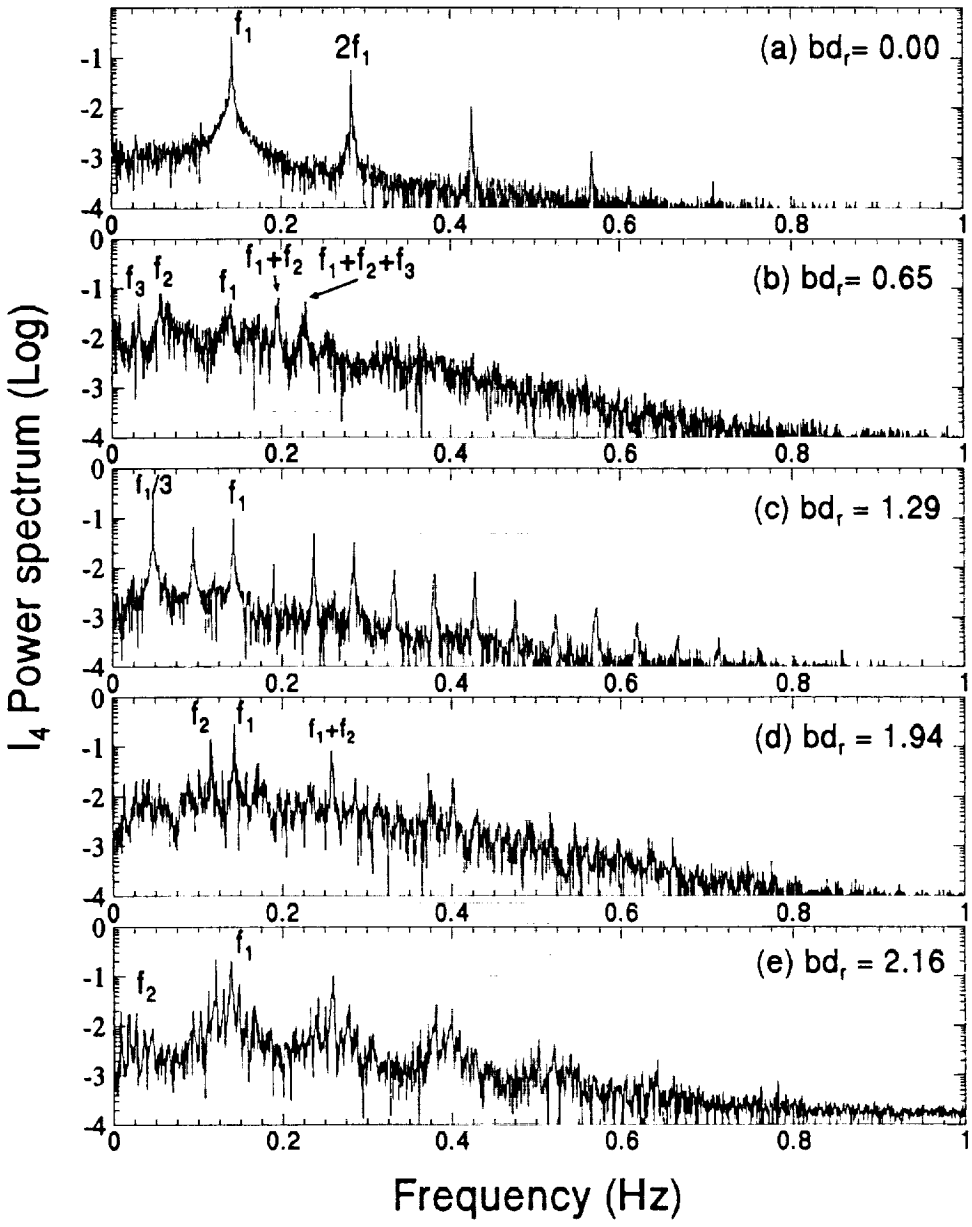

Liu / Indebetouw Fig. 18

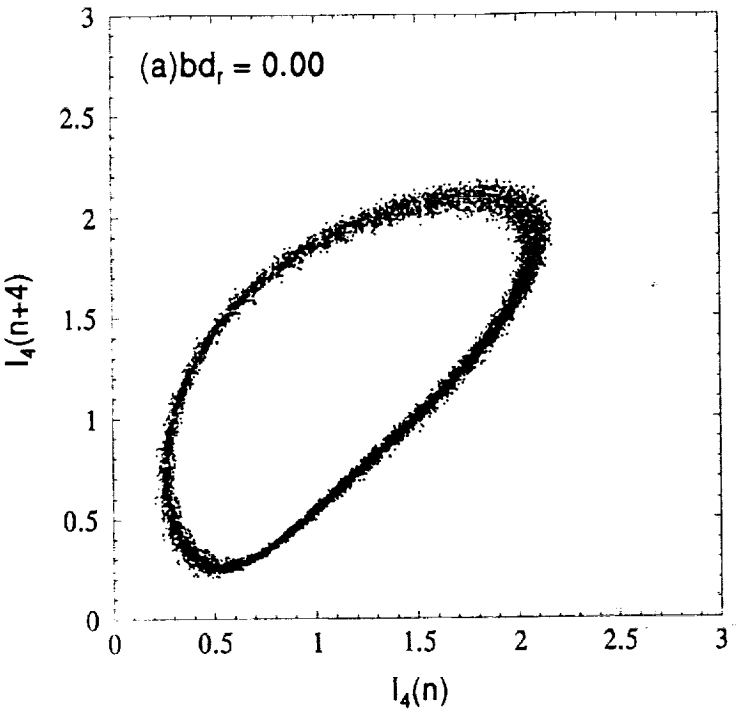

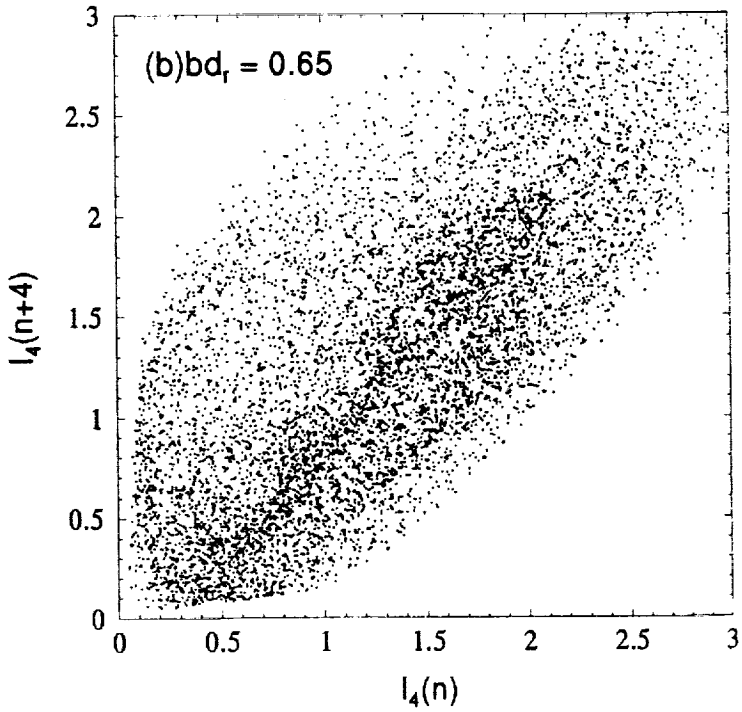

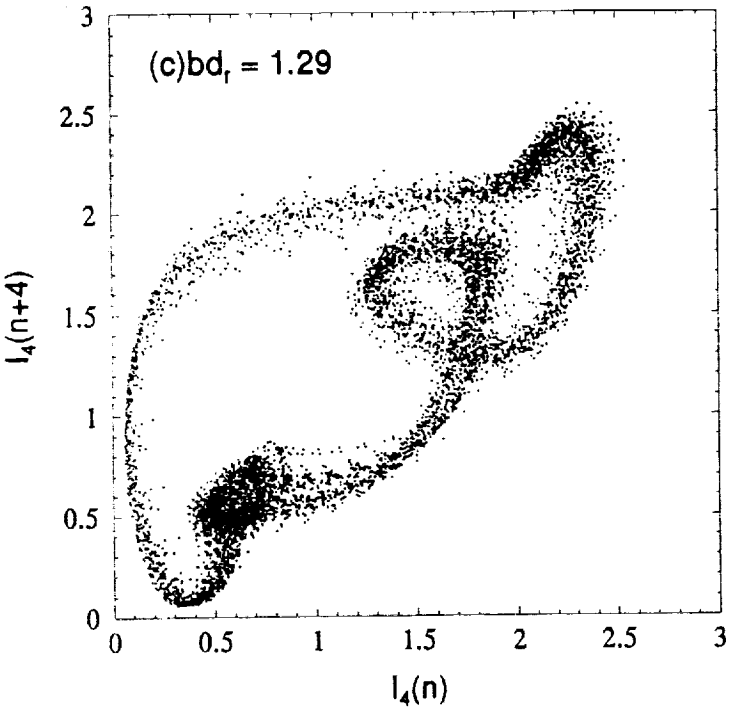

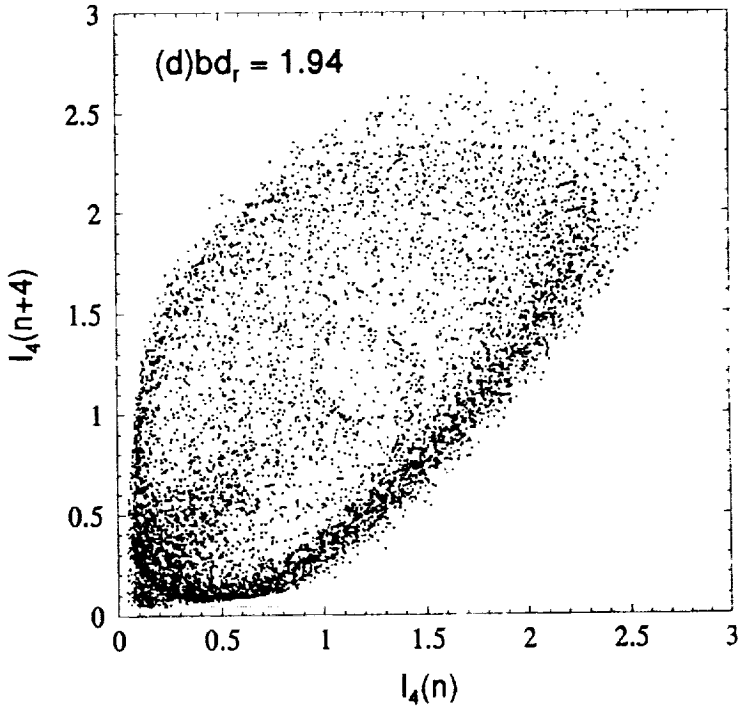

Liu/Indebetouw Fig. 19